ISSP

Activity Report 2002

Contents

PREFACE

- Activity Report -

The ISSP was established in 1957 based on the recommendation of the National Council of Japan to set up a new institute for condensed matter physics. The idea was to establish a top class research institute for experimental and theoretical studies of condensed matter and to promote cooperative research in the field throughout the country. Soon after the inauguration, the name of ISSP became recognized world-wide in the community of condensed matter physics.

Since then there have been two major changes in the history of the institute. The first was the reorganization of the institute in the mid-eighties. The system of divisions consisting of several groups was introduced and the project of the "Physics in extreme conditions", which includes Ultra-High Magnetic Fields, Laser Physics, Surface Physics, Ultra-Low Temperatures, and Very High Pressures, was started. The second major change was the relocation of the ISSP to the new Kashiwa campus which was completed in 2000.

To make the status of the research activities public, new forms were introduced last year: Activity report A for research mostly by the staff of the ISSP and Activity report B for joint research conducted by the ISSP. This is the Activity Report for the fiscal year 2002 in the new style of a single volume but keeping the two sections A and B.

We are happy to receive any comments on the Report for the possible improvement of the research activities of the ISSP.

August 31, 2003

Kazuo Ueda

Director
Institute for Solid State Physics
The University of Tokyo

Section A
Research Highlights

Spin Superstructures in the 1/8-Magnetization Plateau Phase of the 2D Orthogonal Dimer Spin System $SrCu_2(BO_3)_2$

M. Takigawa and Y. Ueda

The discovery of a spin-gap and magnetization plateaus [1] in the quasi two-dimensional orthogonal dimer spin system $SrCu_2(BO_3)_2$ stimulated vast amount of experimental and theoretical activities. The crystal structure realizes a stack of the two-dimensional Shastry-Sutherland spin model, for which the direct product of dimer singlets is the exact ground state. The triplet excitations are known to have an extremely small dispersion width. A striking property of $SrCu_2(BO_3)_2$ is the plateaus in the magnetization vs. field curve at fractional values (1/8, 1/4 and 1/3) of the fully saturated magnetization. It has been argued that the excited triplets with small kinetic energy localize due to repulsive interactions to form superlattices in the plateau phases, i.e., the Mott insulating state or Wigner crystal of magnetic excitations are realized. Since the nuclei on inequivalent Cu-sites in a superstructure should have different magnetic hyperfine fields, which can be observed by NMR, we have performed ^{65}Cu and ^{63}Cu NMR measurements at low temperature (35 mK) in the magnetic field up to 28 T using the facilities in the Grenoble High Magnetic Field Laboratory [2]. The field range covers the first 1/8 plateau state, which occurs for 27 – 28.5 T for the field applied perpendicular to the 2D layers.

Figure 1 shows the Cu NMR spectra at 26 T (inset) and at 27.6 T (main panel). Generally, one type of Cu-sites with a specific value of hyperfine field gives six NMR lines; three lines split by electric quadrupolar interaction for each of two isotopes ^{65}Cu and ^{63}Cu. The spectrum at 26 T can indeed be represented as superposition of such six lines, indicating that the magnetization is largely uniform. At 27.6 T near the middle of the 1/8 plateau, we observed completely different spectrum with large number of sharp peaks distributed over a wide frequency range, providing clear evidence for a magnetic superstructure breaking the translational symmetry.

We found that any satisfactory fitting of the spectrum requires at least 11 Cu sites with different hyperfine fields.

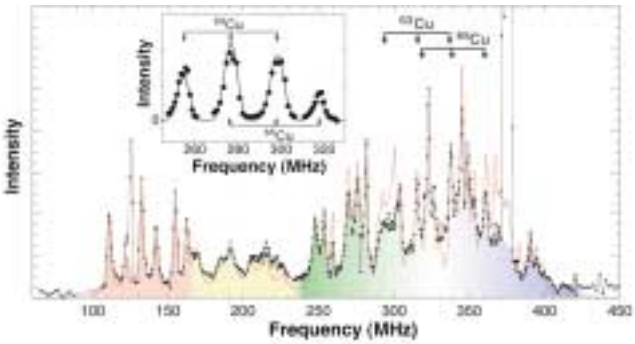

Fig. 1. Cu NMR spectra at 35 mK. The main panel (inset) shows the spectrum in the field of 27.6 (26) T. The red line is the fit with 11 distinct hyperfine fields. The arrows in the main panel show the resonance frequencies for zero hyperfine field. The intense peaks for 371 – 379 MHz (at 126 MHz) is due to ^{11}B (^{10}B) nuclei.

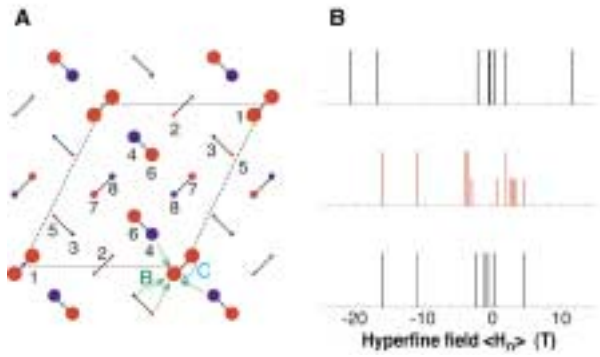

Fig. 2. Right part: Magnetization profile obtained by exact diagonalization of the Shastry-Sutherland model. Red (blue) circles indicate positive (negative) $\langle S_z \rangle$. The circle size represents the magnitude of $\langle S_z \rangle$. Left part: Histogram of the hyperfine field distribution. The middle panel (red) shows results of the fitting of the NMR spectrum (Fig. 2, red line). Long (short) lines indicate that the population of the site is 1/8 (1/16). The top panel is obtained from the calculated profile (right part) assuming only the on-site hyperfine coupling. The bottom panel shows the result when the transferred hyperfine couplings, denoted as B and C in the right part, are adjusted to best reproduce the experimental results.

An example is shown by the red line in Fig. 2. In particular, the six sharp lines in the red zone (105–165 MHz) are ascribed to the sites with the largest magnetization $\langle S_z \rangle$=0.30. Likewise the spectrum in the yellow zone (165-235 MHz) represents another site with $\langle S_z \rangle$=0.20. The rest of the spectrum comes from the sites with smaller hyperfine fields. The distribution of the hyperfine field obtained by this fitting is shown in Fig. 2 (middle panel in the left part). It should be noted that some sites have positive hyperfine fields, i.e., some spins are polarized opposite to the external field. Thus the magnetization oscillates within the unit cell of the superstructure.

By symmetry consideration, we can conclude that the unit cell of the superstructure has the rhomboid shape shown in Fig. 2. The number of inequivalent Cu sites for the rhomboid cell is eight for a single layer, but it may increase up to 16 depending on the pattern of stacking layers along the *c*-axis. We found that other types of unit cell cannot produce as many as 11 sites.

The magnetization profile calculated by exact diagonalization of the Shastry-Sutherland model on a 16-spin cluster of the rhomboid cell is shown in Fig. 2. One can clearly recognize a building unit consisting of one strongly polarized dimmer surrounded by decaying oscillation of magnetization. This resembles the Friedel oscillation near impurities in metals. The distribution of the hyperfine fields derived from the calculatied magnetization profile captures the essential feature of the experimental results, indicating that such a magnetic superstructure is indeed realized in the 1/8 plateau phase.

References

[1] H. Kageyama *et al.*, Phys. Rev. Lett. **82**, 3168 (1999).
[2] K. Kodama *et al.*, Science **298**, 395 (2002).

Authors
K. Kodama, M. Takigawa, M. Horvatic[a], C. Berthier[a,b], H. Kageyama, Y. Ueda, S. Miyahara[b,c], F. Becca[c], and F. Mila[c]
[a]Grenoble High magnetic Field Labrqatory, CNRS-and MPI-KFK,
[b]Laboratorie de Spectrométrie, Université Joseph Fourier,
[c]Institut de Physique Théorique, Université de Lausanne

Novel Superstructures in the Metal Ordered Manganite $YBaMn_2O_6$

Y. Ueda and H. Yoshizawa

The physics of manganese perovskites, $A^{3+}_{1-x}A'^{2+}_{x}MnO_3$, is full of surprises. Emergence of various interesting phenomena such as colossal magnetoresistance is largely due to the versatility of the A site, which forms a wide range of solid solutions between cations with different valences and ionic sizes. This advantage provides us with an opportunity to systematically tune the doping level as well as the tolerance factor. However, such a partial substitution in turn causes a structural disorder, leading to quantitative discrepancy between experiment and theory or even masking some intrinsic features which should inhibit in a 'clean' system.

We have successfully obtained a new manganite perovskite free from a structural distortion, that is, $YBaMn_2O_6$ with the A site ordering in layers along the *c* axis. Among prominent features observed in this material are successive phase transitions containing four phases and an extremely high metal-insulator transition temperature (480 K). In order to obtain insight into the microscopic picture of the paramagnetic insulating (PI) phase below 480 K, we performed transmission electron microscopy (TEM) using JEOL EM2010 operated at 200 kV. At room temperature, we observed a superreflection represented as $q_1=(1/4, 1/4, 0)_p$, see Fig. 1(b). This can be explained in terms of a charge/orbital ordering (COO) of the CE type, which has been mostly observed for the disordered systems with *x* being close to 0.5. However, the $[100]_p$-zone electron diffractions shown in Fig. 1(a) further revealed another modulation, $q_2=(0, 0, 1/4)_p$. Together with the result of Rietveld refinement of powder neutron/x-ray diffractions, we have concluded that the superstructure consists of planes of the CE type built up according to the sequence [ααββ...], see Fig. 2 (a). This superstructure, which has been observed for the first time, should be strongly correlated to the Y/Ba order, since this can make 'orbital' interactions alternated, leading to the quadruplicate periodicity.

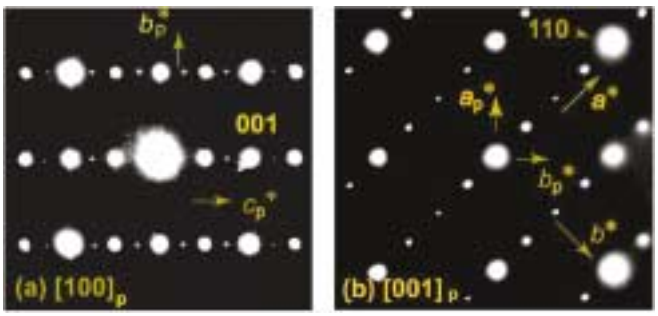

Fig. 1. High-resolution electron diffraction patterns of $YBaMn_2O_6$ at RT obtained along (a) the $[100]_p$-zone and (b) $[001]_p$ -zone axes, where the subscript p denotes the notation for the simple cubic perovskite.

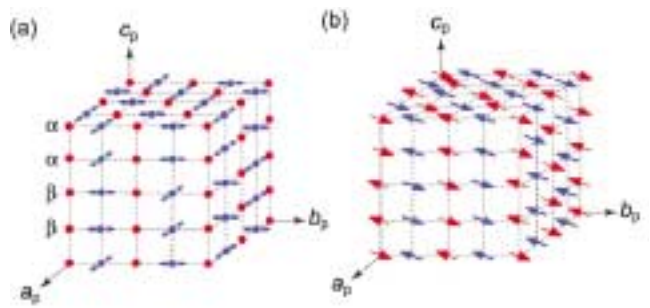

Fig. 2. Proposed charge/orbital and spin ordering patterns in the PI and AFI phases, respectively.

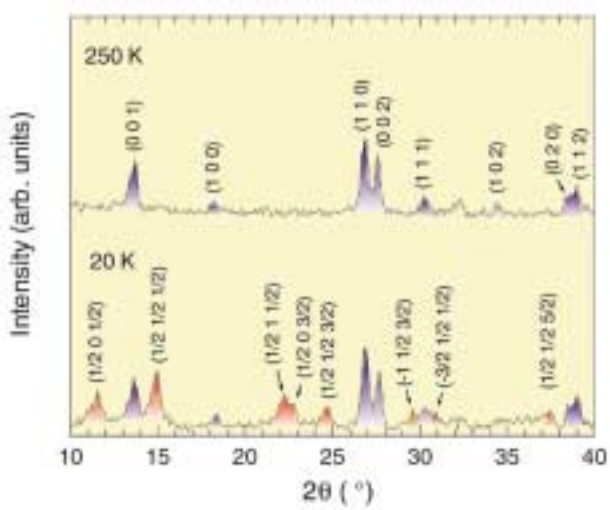

Fig. 3. Neutron diffraction of $YBaMn_2O_6$ at 250 K and 20 K, where the peaks are indexed according to the $\sqrt{2}a_p \times \sqrt{2}b_p \times 2c_p$ unit cell.

Figure 3 compares powder neutron diffraction patterns at 250 K and 20 K, obtained using the Kinken powder diffractometer, HERMES, at the Institute for Material Research, Tohoku University, installed at the JRR-3M reactor in JAERI, Tokai. The magnetic peaks at 20 K in the antiferromagnetic insulating (AFI) phase are characterized by the planes of the CE type with the 4-fold periodicity along the *c* axis. It is natural to consider again that interlayer magnetic interactions become alternated, ferro- and antiferromagnetic, as a result of the A site ordering. Interestingly enough, the q_2 modulation in the PI phase disappears in the AI phase, indicating the COO pattern of either [αααα...] or [αβαβ...]. Transformation of the charge/orbital ordering would be mediated by the spin ordering. In other words, there is a close interplay between spins and orbitals.

References
[1] T. Nakajima *et al.*, J. Phys. Chem. Solid **63**, 913 (2002).
[2] H. Kageyama *et al.*, J. Phys. Soc. Jpn **72**, 241 (2003).

Authors
H. Kageyama, T. Nakajima, M. Ichihara, Y. Ueda, H. Yoshizawa, K. Ohoyama[a]
[a]Tohoku University.

A Light-Emitting Diode Fabricated from Horse-Heart Cytochrome c

H. Tajima and H. Akiyama

Cytochrome c is a relatively low-molecular-weight protein which functions as an electron carrier in the living systems [1]. It belongs to the class of iron-porphyrin-containing proteins, such as hemoglobin, myoglobin, and catalase. The crystal structures of cytochrome c obtained from several living systems are similar at least around the iron-porphyrin which is called as heme c. Figure 1 shows the chemical structure of heme c. In this unit, the Fe atom which may exist in either the oxidized Fe(III) or reduced Fe(II) state, is axially coordinated by histidine (His) and methionine (Met) groups.

We have fabricated ITO/cytochrome c/Al junction from horse-heart cytochrome c. This junction works as a light-

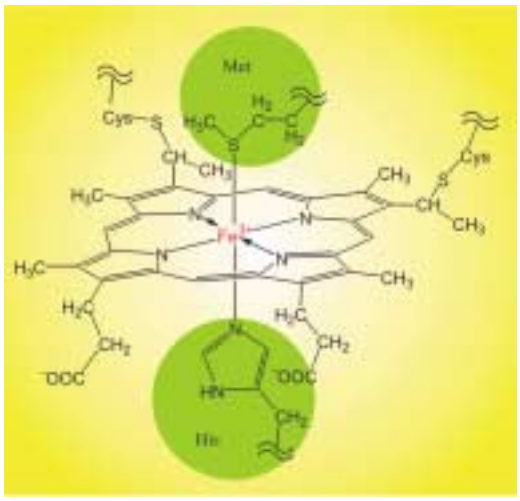

Fig. 1. Molecular structure of heme c (iron porphyrin) in cytochrome c. The abbreviations Met, His denote methionine, and histidine respectively.

emitting diode [2]. Figure 2 shows the absorption spectrum of the cytochrome c film on a glass plate and the typical electro-luminescence (EL) spectrum of the diode.

The EL spectrum exhibits peaks around 530 nm and 690 nm, and a weak shoulder around 410 nm. The 410 nm band corresponds to the Soret band, and the 530 nm band to the Q band. The shape of the EL spectrum is completely different from either the absorption spectrum [3] or the photo-luminescence (PL) spectra [4]. (The oxidized cytochrome c does not show any fluorescence, and the reduced cytochrome c shows a very low yield of the Q band fluorescence when excited in the Soret or Q band.)

Most interesting result obtained in this study is the observation of the strong and broad band around 690 nm in the EL spectrum. This emission band consists of several peaks. The corresponding band very weakly appears in the absorption spectrum. Up to now, there is no report for the observation of this band in the PL experiment. The absorption band around 690 nm is assigned to the charge-transfer excitation between Fe in the porphyrin ring and the Met ligand (See Fig. 1) [3]. Therefore, the appearance of this band in the EL spectrum suggests that the interaction between Fe and Met ligand plays a crucial role in the electrical conduction in the cytochrome c film.

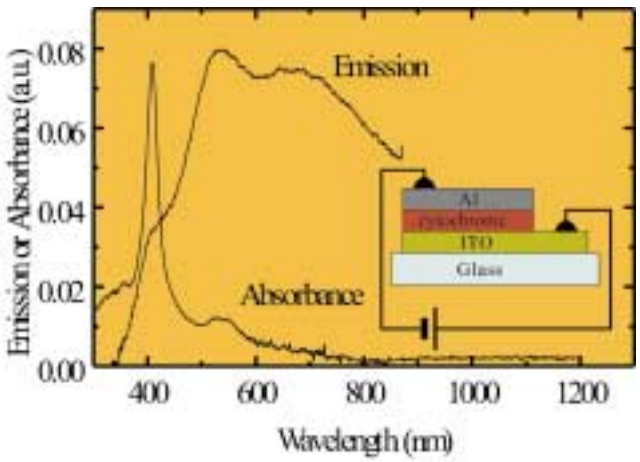

Fig. 2. The typical EL spectrum of the ITO/cytochrome c/Al junction and the absorption spectrum of a cytochrome c film formed on a glass plate.

References
[1] Robert A. Scott and A. Grant Mauk ed., "Cytochrome c", University Science Books, Sausalito, California, 1996.
[2] H. Tajima, S. Ikeda, M. Matsuda, N. Hanasaki, Ji-Won Oh, H. Akiyama, *Solid State Commun.*, **126**, 579 (2003).
[3] W. A. Eaton, R. M. Hochstrasser, *J. Chem. Phys.*, **46**, 2533 (1967).
[4] P. M. Champion, R. Lange, *J. Chem. Phys.*, **73**, 5947 (1980).

Authors
H. Tajima, S. Ikeda, M. Matsuda, N. Hanasaki, Ji-Won Oh, H. Akiyama

Local and Reversible Restructuring on a Ge(001) Surface Driven by STM below 80 K

F. Komori and Y. Yoshimoto

Reversible control of local surface superstructures by STM is expected on the ground state $c(4\times2)$ reconstructed surface of Ge(001) as well as Si(001) because the energy difference between the ground state and the $p(2\times2)$ structure is estimated to a few meV/dimer [1]. We have demonstrated that the surface reconstruction on Ge(001) is locally and reversibly changed between $c(4\times2)$ and $p(2\times2)$ by controlling the sample bias voltage, V_b , of a scanning tunneling microscope (STM) below 80 K. The $c(4\times2)$ structure is observed with V_b<-0.7 V while the $p(2\times2)$ with V_b>+0.8 V. Moreover, the both structures can be kept under scanning the surface with $|V_b|$<0.6 V after fixing the surface structure of a local area by scanning there with a higher $|V_b|$. Figures 1 shows successive local modifications of the surface. After taking the image shown in Fig. 1(a), the area A in the figure was scanned with V_b=0.8 V to change from $c(4\times2)$ to $p(2\times2)$. The result is shown in Fig. 1(b). The change along the dimer row continued to the outside of the scanning area. Then we scanned the area B in Fig. 1(b) to form another $p(2\times2)$ area as shown in Fig. 1(c). The reverse change from $p(2\times2)$ to $c(4\times2)$ was done by scanning the area C in Fig. 1(c) with V_b=-0.7 V. In this case, we had to scan all of the desired $p(2\times2)$ area because the change to $c(4\times2)$ was limited nearby the area of the scanning along the dimer row. The

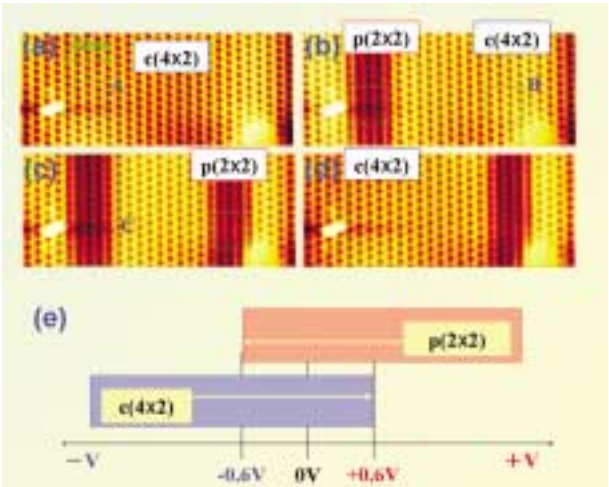

Fig. 1. (a-d) Successive STM images of the same area (22.5 × 10 nm^2) of a Ge(001) surface at 80 K with V_b=-0.2V. The square areas "A" in (a) and "B" in (b) were scanned with V_b=0.8 V to change the local structure from $c(4\times2)$ to $p(2\times2)$ after taking each image. The surface after scanning "A" is shown in (b), and that after scanning "B" is in (c). The rectangular area "C" in (c) was scanned with V_b=-0.7 V to change it from $p(2\times2)$ to $c(4\times2)$. The surface after scanning the area "C" is shown in (d). (e) A schematic showing the observed structures depending on the bias voltage and the change direction.

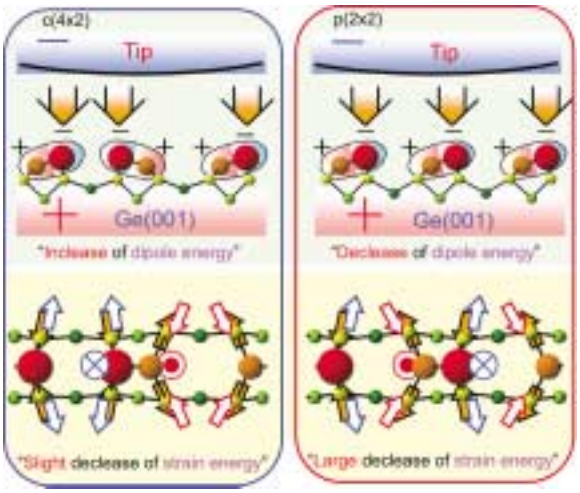

Fig. 2. When the surface is positively biased under the STM tip, the negatively charged upper-atoms of the dimers are electro-statically pushed toward the subsurface by the tip, and the lower-atoms are pulled toward the tip. Consequently, the dimer buckling becomes smaller. This makes the difference of the subsurface strain energy between $c(4\times2)$ and $p(2\times2)$ structures smaller than that of the dipole energy among buckled dimers. Thus for the positively biased surface, the $p(2\times2)$ structure is favored by the gain of the dipole energy, and can be the ground state.

annihilation of $p(2\times2)$ is shown in Fig. 1(d). The observed structure is summarized in Fig.1(e). The bistability between $p(2\times2)$ and $c(4\times2)$ on V_b is attributed to the changes in two competing energies determining the structure; the electric dipole energy among the Ge dimers, and that of the subsurface lattice strain. The upper atom of the Ge dimer is negatively charged, and the dipole energy for $p(2\times2)$ structure is smaller than that for $c(4\times2)$. On the other hand, the strain energy for $p(2\times2)$ is larger than that for $c(4\times2)$. Both are affected by the electric field between the tip and the surface as schematically shown in Fig.2. For the positively biased surface, the $p(2\times2)$ structure is favoured by the gain of the dipole energy, and can be the ground state. On the other hand, under the negative V_b, the buckling of the dimers is increased by the electric field, and the $c(4\times2)$ structure is more favoured. The current dependence of the transition indicates that an inelastic scattering process during the electron tunnelling induces the transition under the electric field by STM.

Reference
[1] Y. Yoshimoto *et al*., Phys. Rev. B**61**, 1965 (2000).

Authors
Y. Takagi, Y. Yoshimoto, K. Nakatsuji and F. Komori

Development of an Opposed-Anvil Type Apparatus for High Pressure-Temperature Melting Experiments

T. Yagi

A high pressure-temperature apparatus capable for uniform melting experiments at very high pressures is developed. Use of double stage multi-anvil apparatus made it possible to perform well controlled high pressure-temperature experiments up to about 25 GPa. Although the pressure range is further extended recently by the use of sintered diamond as anvil material, multi-anvil system has various difficulties when experiments above 40 GPa are tried. Opposed-

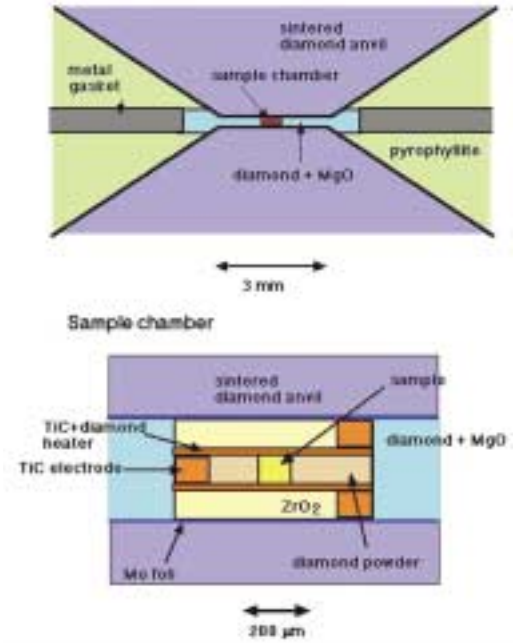

Fig. 1. Schematic diagram of the whole view (above) and sample chamber (below) of the opposed-anvil type apparatus using sintered diamond.

anvil type apparatus has much simple structure and has high potential to extend pressures, as is clear from diamond-anvil apparatus. In diamond anvil, however, uniform and stable heating of the sample is extremely difficult, because of the intrinsic nature of laser heating. Here we used an opposed-anvil apparatus adopting sintered diamond as anvil material, and developed sample assembly to make uniform and stable heating by resistance heating. Fig. 1 is the schematic diagram of the sample assembly. The heater material is a mixture of TiC and diamond powder hardened by adding small amount of epoxy resin. All the small parts were prepared by a laser machining system, which enables us to make small size machining with high precision. Heater material, sample chamber, and electrodes thus prepared are stacked in the hole of the pressure transmitting medium made of a mixture of MgO and diamond, and then compressed by two sintered diamond anvils. By running an electric power of about 200 W to this assembly, temperature higher than 2000 K can be achieved. Fig.2 is an example of the sample recovered from

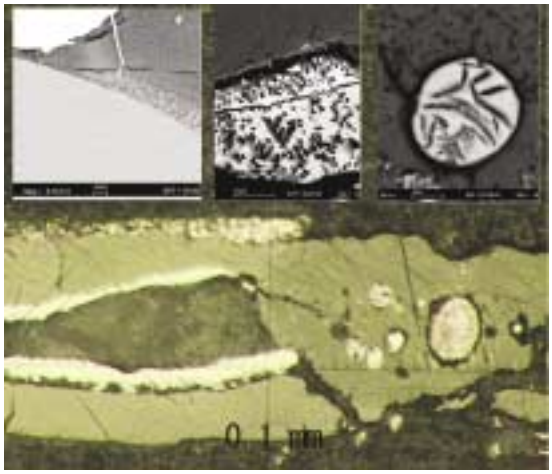

Fig. 2. SEM photograph of the cross section of the sample recovered from high pressure-temperature experiment. Three photographs at the top are the enlarged pictures of various small parts. Various features of crystal growth, formation of immiscible liquid, and reactions among ZrO_2, TiC, Mo, and Re can be seen.

high pressure-temperature experiments, which show a mixture of TiC, ZrO_2, Mo, and Re, melted at pressures above 30 GPa. This is a preliminary test and further extension of the pressure range is expected but this figure show high potential to make melting experiment at very high pressure using this new apparatus. Further development to make quantitative analysis of pressure and temperature are in progress by combining with a synchrotron radiation.

Authors
T. Yagi, H. Goto, D. Rubie[a], and D. Frost[a]
[a]University of Bayreuth

Superconducting Gap Structure of Unconventional Superconductors

Y. Matsuda

Nodes of the superconducting gap functions are often important hallmarks for unconventional superconductors. Despite the fact that the gap functions have immediate bearings on the pairing mechanism, we have for most of the unconventional superconductors been lacking detailed knowledge on its structure, especially the direction and type of nodes present. A recent series of experiments carried out by our group have demonstrated that the low temperature thermal transport measurements in magnetic field rotated in various directions is a powerful tool for probing such nodal structures. We proved the superconducting gap structures of 2D superconductors (1) spin triplet Sr_2RuO_4, (2) heavy fermion $CeCoIn_5$, (3) organic κ-$(BEDT\text{-}TTF)_2Cu(NCS)_2$, the 3D superconductor (4) borocarbide YNi_2B_2C and (5) the new heavy fermion $PrOs_4Sb_{12}$, by the low temperature thermal transport measurements. The gap functions of Sr_2RuO_4, $CeCoIn_5$ and κ-$(BEDT\text{-}TTF)_2Cu(NCS)_2$, have line nodes which are shown in Figures below. We also obtained evidence for the existence of point nodes for YNi_2B_2C and $PrOs_4Sb_{12}$ shown in Figures below. For $PrOs_4Sb_{12}$ we observed an unexpected multiple superconducting phases.

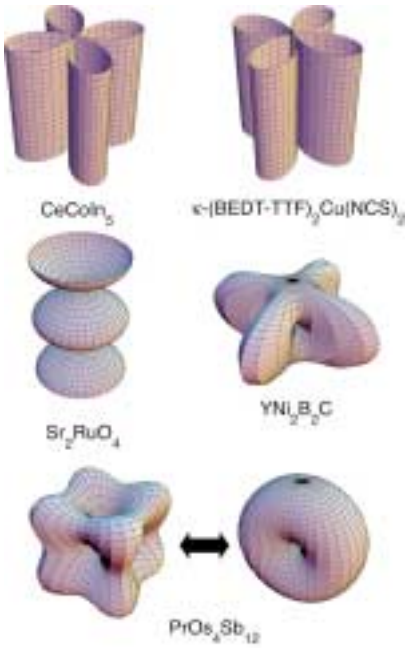

Fig. 1. Superconducting gap structure of unconventional superconductors, which are proved by the low temperature thermal transport measurements.

References
[1] K. Izawa *et al*., Phys. Rev. Lett. **86**, 2653 (2001).
[2] K. Izawa *et al*., Phys. Rev. Lett. **84**, 057002 (2001).
[3] K. Izawa *et al*., Phys. Rev. Lett. **88**, 027002 (2002).
[4] K. Izawa *et al*., Phys. Rev. Lett. **89**, 137006 (2002).
[5] K. Izawa *et al*., Phys. Rev. Lett. **90**, 117001 (2003).

Authors
Y. Matsuda and K. Izawa

Field-Induced Ordering in the Heavy-Electron Superconductor $PrOs_4Sb_{12}$

T. Sakakibara

The cubic skutterudite compound $PrOs_4Sb_{12}$ has recently been attracting much interest because it is the first Pr-based heavy-electron superconductor that is most probably of unconventional type [1,2]. In $PrOs_4Sb_{12}$, the Van Vleck behavior of the magnetic susceptibility suggests that the crystalline-electrical-field (CEF) ground state is either a non-magnetic doublet or a singlet [3]. The heavy electron behavior has often been discussed in relation to a quadrupolar Kondo effect assuming the doublet ground state of Pr^{3+}[1,3]. Identification of the CEF ground state of this system is of importance for understanding the formation of the heavy-electron state in this system, but the situation seems to be still controversial [3,4]. In order to gain further insight into this issue, we examined the field-induced ordering in $PrOs_4Sb_{12}$ [5] which has recently been revealed for H||[100] by the specific heat measurements [4]. Since this type of phase diagram has never been observed in Ce-based heavy fermion compounds, the origin is considered to be specific to the 4*f* electronic state of Pr^{3+}.

Field-induced phase transitions can be seen most clearly in the differential susceptibility data dM/dH, some examples of which are shown in Fig. 1 for H||[110]. Here the transition to the ordered phase (A-phase) is marked by a jump in dM/dH at ~50 kOe (thick arrows). A transition from the A-phase to a paramagnetic state can also be seen at ~110 kOe. For this direction, we observed additional peaks in dM/dH at H_1 and H_2 within the A-phase, possibly due to certain changes in the ordered structure.

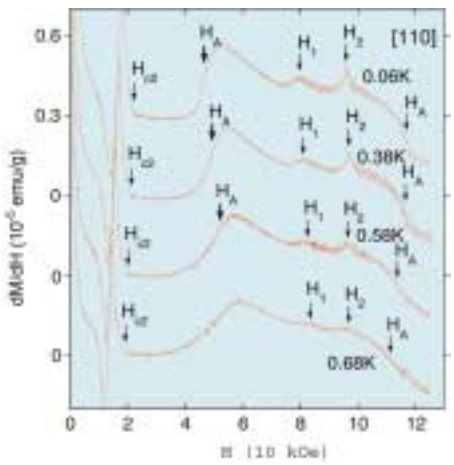

Fig. 1. Differential susceptibility of $PrOs_4Sb_{12}$ for H||[110], obtained at T = 0.06 K~0.68 K. The field-induced ordering is marked by a jump in dM/dH as shown by thick arrows. Two distinct peaks are observed in dM/dH at H_1 and H_2 within the ordered phase, suggesting some changes in the ordered structure. The sharp structures below H_{c2} are due to the peak effect. Small oscillations seen above 8 T are the de Haas-van Alphen effect.

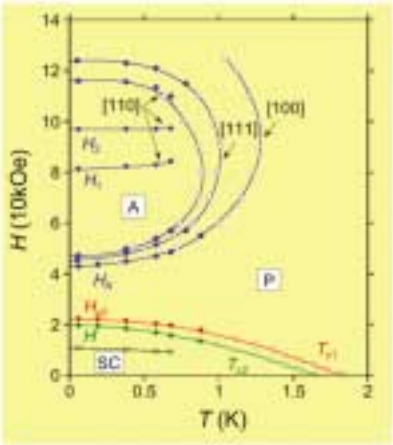

Fig. 2. *H-T* phase diagram of $PrOs_4Sb_{12}$ with *H*∥[100], [110] and [111] as indicated. Field-induced ordered phase (A-phase) is observed for all the principal directions. Double superconducting transition is observed at low field. No strong anisotropy is found for the superconducting state.

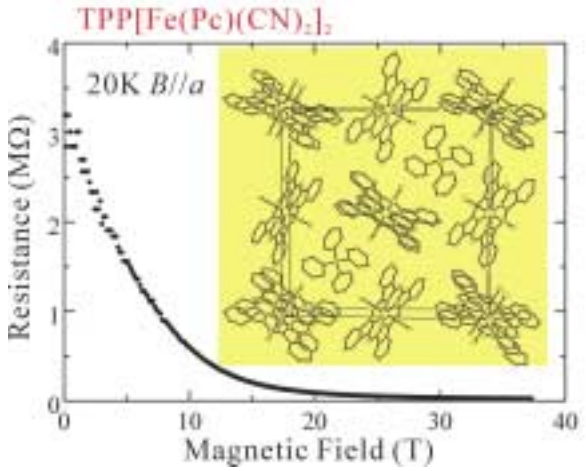

Fig. 1. Field dependence of the electrical resistance of TPP[Fe^{III}(Pc)$(CN)_2]_2$ at 20 K. The field is applied parallel to the *a*-axis. The inset shows the crystal structure. Note that the resistance decreases less than 1 % of the zero-field value.

We continued the measurements also for the other directions, and obtained the field-temperature phase diagrams as shown in Fig.2 [5]. It should be emphasized that the ordered phase is observed for all the principal directions. The transition temperature $T_A(H)$ is somewhat anisotropic, being lowest (highest) for *H*∥[110] ([100]). We also confirmed that the A-phase closes at high fields, except for *H*∥[100] where the upper border was not observed because of the present experimental limitation. The field-induced ordering is considered to result from a level crossing of the Zeeman split CEF states as well as intersite multipole interactions. It can be shown that the presence of A-phase, irrespective of field direction, is incompatible with the doublet ground state model, indicating that the CEF ground state of this system is a Γ_1 singlet [5]. This implies that the CEF excited state (triplet) existing at ~6 K above the ground state is responsible for the heavy-electron formation. As for the superconducting state, we observed that the double transition at T_{c1}=1.85 K and T_{c2}=1.75 K recently reported in the specific heat measurement [3] extends to lower temperatures down to T≈0 [5]. $PrOs_4Sb_{12}$ exhibits rich phase diagrams. Further experiments are in progress to understand this interesting system.

References
[1] E.D. Bauer *et al*., Phys. Rev. B **65**, 100506(R) (2002).
[2] K. Izawa *et al*., Phys. Rev. Lett. **90**, 117001 (2003).
[3] R. Vollmer *et al*., Phys. Rev. Lett. **90**, 057001 (2003).
[4] Y. Aoki *et al*., J. Phys. Soc. Jpn. **71**, 2098 (2002).
[5] T. Tayama *et al*., J. Phys. Soc. Jpn., **72**, 1516 (2003).

Authors
T. Tayama, T. Sakakibara, H. Sugawara[a], Y. Aoki[a] and H. Sato[a]
[a]Department of Physics, Tokyo Metropolitan University

Giant Negative Magnetoresistance in TPP[Fe^{III}(Pc)$(CN)_2]_2$ and the Related Compounds

H. Tajima

A search for a new function based on the interplay between local magnetic moments and conduction electrons is a current topic in the field of molecular conductors. Most of research works concern charge-transfer complexes composed of inorganic anions having local magnetic moments and molecular donors affording π-conduction electrons. The key to synthesize such compounds is the strength of the *d*-π interaction (the interaction between local magnetic moments and π-conduction electrons). In the case of the charge-transfer complexes above mentioned, however, this strength is determined by the crystal structure whose design is still beyond control. One of the ways to solve this problem is to synthesize charge transfer complexes by using the molecules, where the strong *d*-π interaction is self-contained. In this context, we are studying a new series of charge-transfer salts containing the axial-substituted phthalocyanine (Pc), [Fe^{III}(Pc)$(CN)_2]^-$, where the strong *d*-π interaction is self-contained. Interestingly, all the conducting salts containing [Fe^{III}(Pc)$(CN)_2]^-$ (TPP[Fe^{III}(Pc)$(CN)_2]_2$ [1, 2], PXX[Fe^{III}(Pc)$(CN)_2$] [3], $PTMA_x$[Fe^{III}(Pc)$(CN)_2]^-$ y(MeCN) [4], TPP[$Fe^{III}_{0.3}Co^{III}_{0.7}(Pc)(CN)_2]_2$[5]) exhibit the anisotropic giant negative magnetoresistance.

Recently, we found the resistivity of TPP[Fe^{III}(Pc)$(CN)_2]_2$ decreases down to less than 1 % of the zero-field value under the magnetic field of 38 T. (See Figure 1.) This decrease is not due to a phase transition.

Figure 2 shows the normalized resistivity of TPP[Fe^{III}(Pc)$(CN)_2]_2$ plotted versus magnetic field at vari-

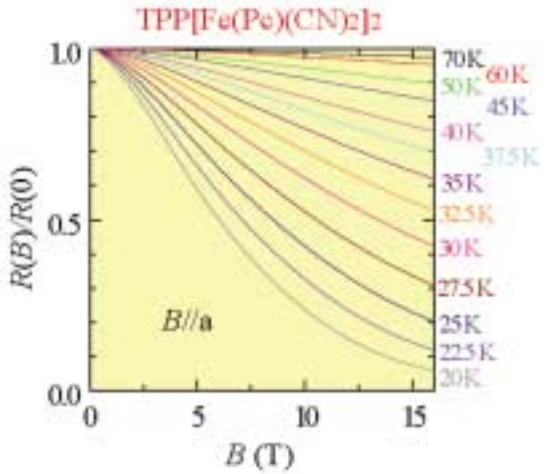

Fig. 2. Normalized resistivity of TPP[Fe^{III}(Pc)$(CN)_2]_2$ plotted versus field at various temperatures. Note that the negative magnetoresistance is observed even at 70 K.

ous temperatures. As can be seen from this figure, the negative magnetoresistance is observed even at 70 K.

References

[1] M. Matsuda, T. Naito, T. Inabe, N. Hanasaki, H. Tajima, T. Otsuka, K. Awaga, B. Narymbetov, and H. Kobayashi, *J. Mater. Chem.* **10**, 631 (2000).
[2] N. Hanasaki, H. Tajima, M. Matsuda, T. Naito, T. Inabe, *Phys. Rev. B* **62**, 5839 (2000).
[3] N. Hanasaki, M. Matsuda, H. Tajima, T. Naito, T. Inabe, *Synth. Met.*, **133**, 519 (2003).
[4] M. Matsuda, T. Naito, T. Inabe, N. Hanasaki, H. Tajima, *J. Mater. Chem.* **11**, 2493 (2001).
[5] H. Tajima, N. Hanasaki, M. Matsuda, F. Sakai, T. Naito, T. Inabe, *J. Solid State Chem.*, **168**, 509 (2002).

Authors

N. Hanasaki, M. Matsuda, K. Masuda, H. Tajima, E. Ohmichi, T. Naito[a], T. Inabe[a]

[a]Division of Chemistry, Graduate School of Science, Hokkaido University

Metallic States in the Novel Hydrogen-Bonded System: β''-(CnDT-EDO-TTF)$_2$X (n = 5, 6, 7)

H. Mori

In molecular conductors, it is of a great importance to control a molecular arrangement, which determines the electronic state of the charge transfer (CT) salt. However, the intermolecular interactions are generally small, so that to obtain only the desired phase among the polymorphism is usually difficult.

In organic solids, the hydrogen bond is known to afford relatively large intermolecular interactions [1], by use of which a molecular arrangement would be preferentially constructed. Moreover, the strength and dimensionality of the hydrogen-bonded network would be controllable by the

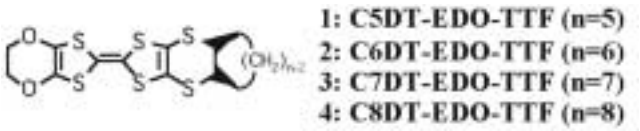

Fig. 1. Molecular structures of CnDT-EDO-TTF.

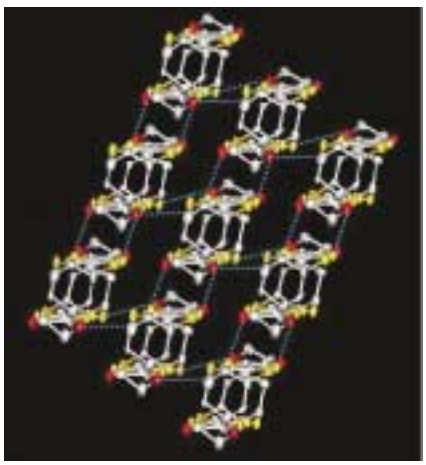

Fig. 2. Crystal structure of β''-(C6DT-EDO-TTF)$_2$PF$_6$. The intermolecular CH…O contacts (< 2.89 Å) are indicated by the dotted lines. The hydrogen network spreads in the two-dimensional (2D) plane. Consequently, the peudo-2D electronic state is constructed.

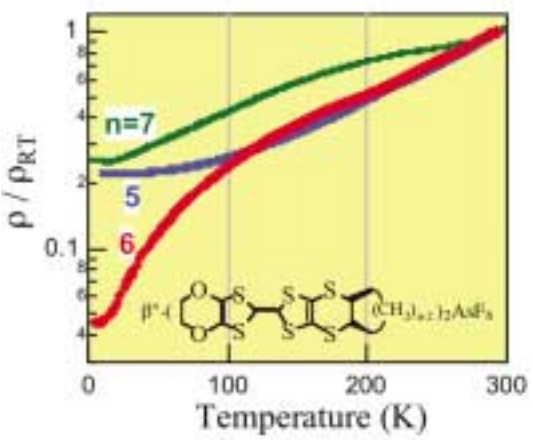

Fig. 3. Temperature dependences of electrical resistivities for β''-(CnDT-EDO-TTF)$_2$AsF$_6$. The resistivity of the n = 5 salt is proportional to $\sim T^{2.4}$, suggesting the electron-correlated system. The resistivity change from the n = 6 to the 5 salt indicates the chemical pressure effect in substitution of the steric hindrance part of the molecule.

introduction of a steric hindrance part to the molecule, so as to regulate the electronic state from an insulator, a superconductor, to a metal. Therefore, we synthesized a novel series of CnDT-EDO-TTF (**1 – 4;** n = 5 - 8 in Fig. 1) containing cycloalkylene and ethylenedioxy groups, owing to function as a hydrogen bond (CH··O) and a steric hindrance, and carried out the crystal structure analyses, the band calculations, and electrical conductivities of **D**$_2$X (**D** = **1 - 4**) to clarify the electronic state of this system.

The crystal structure analyses of the prepared single crystal, β''-**2**$_2$PF$_6$, revealed the layered structure composed of the donor and the anion sheets. In the donor layer, the CH···O contacts (< 2.89 Å) between cycloalkylene and ethylendioxy groups are observed and the two-dimensional hydrogen-bonded network spreads in the *ac* plane. (Fig. 2) Consequently, the calculated overlaps along the molecular 0º, 30º, and 60º directions are large enough to construct a pseudo-two dimensional Fermi surface. In addition, the analogues, β''-(CnDT-EDO-TTF)$_2$X (n = 5, 6, 7, X = PF$_6$, AsF$_6$), have the similar donor arrangement in use of hydrogen-bonded interactions.

In order to compare the electronic states of β''-(CnDT-EDO-TTF)$_2$AsF$_6$ (n = 5, 6, 7), the electrical resistivity measurements were carried out. As shown in Fig. 3, the resistivity of β''-**1**$_2$AsF$_6$ is proportional to $\sim T^{2.4}$, suggesting the electron-correlated system. The typical example of the correlated system is κ-ET$_2$X [2]. In the most pressurized condition, the resistivity behavior corresponds to that of the n = 5 salt. With releasing the pressure, the convex resistivity curve like that of the n = 6 salt was observed. Therefore, the chemical pressure effect could be realized in β''-(CnDT-EDO-TTF)$_2$X (n = 5, 6) in the two-dimensional hydrogen-bonded network.

References

[1] G. R. Desiraju, Acc. Chem. Res., **29**, 441-449 (1996).
[2] H. Urayama-Mori, H. Yamochi, G. Saito, K. Nozawa, T. Sugano, M. Kinoshita, S. Sato, K. Oshima, A. Kawamoto, and J. Tanaka, Chem. Lett., **1988**, 55; K. Kanoda, Physica C, **282-287**, 299 (1997).

Authors

H. Suzuki, M. Suto, K. Yamashita, T. Maejima, S. Kimura, H. Mori, H. Moriyama[a], Y. Nishio[a], and K. Kajita[a]

[a]Toho University

Theory of Nonequilibrium Kondo Effect in a Quantum Dot

K. Ueda

Recently it has been established that the Kondo effect is relevant to the transport property through a quantum dot. Clearly a new feature of the Kondo transport compared with the usual Kondo effect of magnetic impurities is the nonequilibrium nature, since the current is measured with a finite bias voltage.

To treat the correlation effect, the second order perturbation theory with respect to the Coulomb interaction U in the dot [1] has been used as one possible method. According to this theory the Kondo resonance is simply suppressed by a finite voltage and does not show any particular structure in the nonequilibrium situation. However, it is not clear whether the second-order perturbation theory works well in the nonequilibrium conditions. On the other hand, the noncrossing approximation (NCA) has predicted the double peak structure at the chemical potentials of both leads [2]. This result was obtained also by other approaches, the equation of motion [2], a real-time diagrammatic formulation [3] and scaling method [4]. Moreover the splitting of the Kondo peak was successfully observed by introducing a potential difference in the source lead [5]. These are favorable results for the splitting of the Kondo resonance by a finite bias voltage.

It is still not clear how the effects of the double peak structure, if it is true, appear in the differential conductance. Moreover concerning the NCA it is well known that the analyticity is broken in the low temperature limit. Thus one cannot discuss the conductance in the unitary limit by the NCA. In this situation it is clearly necessary to study the nonequilibrium Kondo effects by a better theoretical approach.

We have developed a theory of quantum transport through a dot under finite voltage by using the perturbation theory up to the fourth order of U based on the Keldysh formalism.

1) The density of states is shown in Fig.1 in units of $1/\pi\Gamma$. With a small voltage, the Kondo peak is suppressed but still keeps a single peak with additional broadening. A remarkable result of the theory is that the Kondo peak splits into double peaks near the chemical potentials of the two leads when the bias voltage exceeds the Kondo temperature, k_BT_K.
2) In Fig.2 the differential conductance as a function of bias voltage is shown in units of $2e^2/h$ for various values of U/Γ. It is seen that the new peak appears for large U, $U/\Gamma = 6$ between the zero-bias peak and the broad peak at around $eV \sim U$. The new peak appears when the bias voltage exceeds the Kondo energy.
3) It may be possible to speculate that the present results are relevant to the 0.7 conductance anomaly. In experiment [6], it is clearly demonstrated that the crossover between the region of the conductance of the unitary limit and the 0.8 plateau region takes place around the Kondo temperature. This result is consistent with the prediction of the present study.

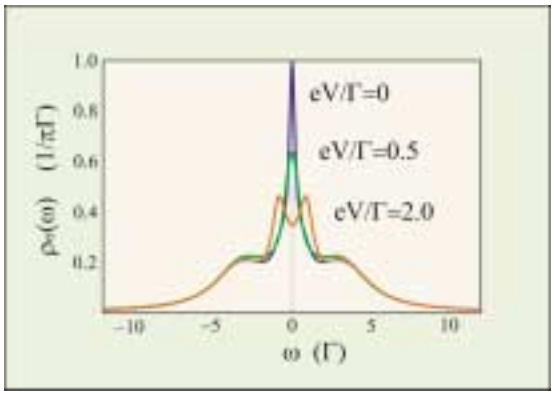

Fig. 1. The density of states are shown in units of $1/\pi\Gamma$ for various eV/Γ where $U/\Gamma = 6$.

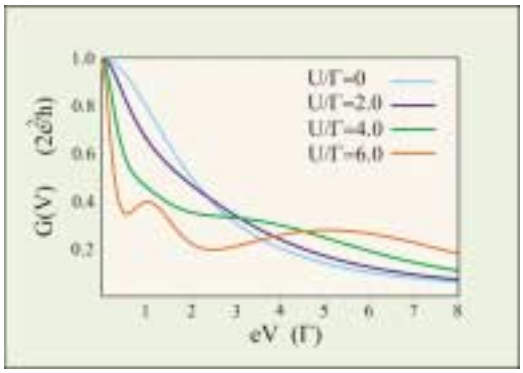

Fig. 2. The differential conductance in the unit of $2e^2/h$ is denoted about various values of U/Γ. The zero-bias peaks reach to $2e^2/h$ in the unitary limit for the symmetric case. The anomalous peak in $eV > k_BT_K$ is developed with increasing U/Γ in addition to the zero bias peak.

References
[1] S. Hershfield *et al*., Phys. Rev. Lett. **67**, 3720 (1991); Phys. Rev. B. **46**, 7046 (1992)
[2] Y. Meir, N. S. Wingreen and P. A. Lee, Phys. Rev. Lett. **70**, 2601 (1993); N. S. Wingreen and Y. Meir, Phys. Rev. B. **49**, 11040 (1994).
[3] J. König *et al*., Phys. Rev. B **54**, 16820 (1996).
[4] A. Rosch *et al*., Phys. Rev. Lett. **87**, 156802 (2001); cond-mat/0202404.
[5] S. De Franceschi *et al*., Phys. Rev. Lett. **89**, 156801 (2002).
[6] S. M. Cronenwett *et al*., Phys. Rev. Lett. **88**, 226805 (2002).

Authors
T. Fujii and K. Ueda

Thermodynamics and Correlation Functions of Spin-1/2 One-Dimensional Heisenberg Models

M. Takahashi

The spin-1/2 Heisenberg chain $H = J\sum_{j=1}^{L} \boldsymbol{S}_j \cdot \boldsymbol{S}_{j+1}$ is the one of the fundamental models which has been extensively investigated in the study of the magnetism in low dimensions. The model is solvable by Bethe Ansatz method and lots of physical quantities have been calculated exactly over past 70 years [1]. However, many new developments are still being reported continuously. Among them we have achieved two significant progresses recently.

Thermodynamics and High-Temperature Expansion

The thermodynamics of the spin-1/2 Heisenberg chain has been studied traditionally through the Thermodynamic Bethe Ansatz (TBA) equations and the Quantum Transfer Matrix (QTM) method [1]. Both methods finally result in a kind of non-linear integral equations among some auxiliary functions, from which we can evaluate the free-energy of the system. Quite recently we have found one more different integral equation, which determines the free-energy rather directly [2]. The new integral equation consists of one unknown function and is quite simple. Particularly we have

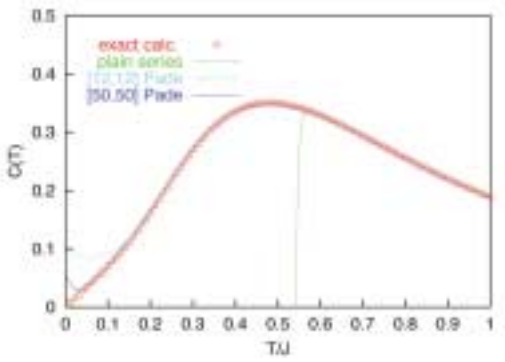

Fig. 1. Specific heat for the spin-1/2 anti-ferromagnetic Heisenberg chain. [12,12] and [50,50] Padé are calculated from the high temperature expansion of the order $(J/T)^{24}$ and $(J/T)^{100}$, respectively.

found the equation is extremely powerful for the calculation of the high temperature expansion (HTE) of the free-energy as well as other thermal quantities [3]. Actually by expanding the integral equation with respect to J/T, we could obtain the HTE of the specific heat $C(T)$ and the magnetic susceptibility $\chi(T)$ up to the order of $(J/T)^{100}$. If we use the standard linked-cluster algorithm, only the order of $(J/T)^{24}$ is attainable. Thus our results will present the fundamental benchmarks for the application of the HTE, especially to the quantum critical phenomena. Fig.1 and Fig.2 plot the specific heat and the magnetic susceptibility of the spin-1/2 anti-ferromagnetic (J>0) Heisenberg chain, calculated from the numerical solution of the integral equation. The HTEs are also shown in the plots. Note that, as the plain HTE series always diverge around T/J =0.55, we have applied the Padé approximation to the HTE series. Particularly the [50,50] Padé's are obtained from our HTE results of the order $(J/T)^{100}$. One can see our new [50,50] Padé approximants provide the precise values for $C(T)$ and $\chi(T)$ even in very low temperature region.

Exact Calculation of Correlation Functions

Evaluation of the correlation functions for the interacting systems are critically significant but very difficult problem even for the exactly solvable models. As for the antiferromagnetic Heisenberg chain $H = J\sum_{j=1}^{L} S_j \cdot S_{j+1} \quad (J > 0)$, only the nearest-neighbor and the next nearest-neighbor correlation are known for a long time as [1]

$$\langle S_j \cdot S_{j+1} \rangle = \tfrac{1}{4} - \ln 2,$$

$$\langle S_j \cdot S_{j+2} \rangle = \tfrac{1}{4} - 4\ln 2 + \tfrac{9}{4}\zeta(3).$$

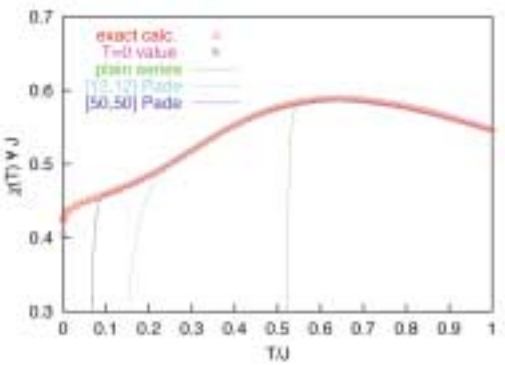

Fig. 2. Magnetic susceptibility for the spin-1/2 anti-ferromagnetic Heisenberg chain. [12,12] and [50,50] Padé are calculated from the high temperature expansion of the order $(J/T)^{24}$ and $(J/T)^{100}$, respectively.

Here $\zeta(s)$ is the Riemann zeta function. However, we have recently succeeded in calculating the third neighbor correlation function [4]

$$\langle S_j \cdot S_{j+3} \rangle = \frac{1}{4} - 9\ln 2 + \frac{37}{2}\zeta(3) - 14\zeta(3)\ln 2 - \frac{9}{2}\zeta(3)^2 - \frac{125}{8}\zeta(5) + 25\zeta(5)\ln 2.$$

Our calculation is based on the multiple integral representation of the correlation functions. Although the integral representation itself was obtained already in 1990's by Jimbo et al, its analytical evaluation has not been accomplished until quite recently. However, Boos and Korepin could devise a general method to evaluate the multiple integrals recently. We have found their method is actually applicable to the calculation of arbitrary correlation functions of the spin-1/2 Heisenberg chain. Furthermore we could generalize the method to the Heisenberg XXZ chain (anisotropic extension of the Heisenberg chain) in [5].

References

[1] M. Takahashi, *Thermodynamics of One-Dimensional Solvable Models* (Cambridge University Press, Cambridge 1999).
[2] M. Takahashi, in *Physics and Combinatrics*, eds. A.K. Kirillov and N. Liskova, p299-304, (World Scientific, Singapore, 2001).
[3] M. Shiroishi and M. Takahashi, Phys. Rev. Lett. **89** 117201 (2002).
[4] K. Sakai, M. Shiroishi, Y. Nishiyama and M. Takahashi, Phys. Rev. E. in press.
[5] G. Kato, M. Shiroishi, M. Takahashi and K. Sakai, J. Phys. A : Math. Gen. in press.

Author
M. Takahashi

Interplay of Orbital, Spin and Lattice in Titanium Oxides

M. Imada

Magnetic orders are frequently controlled and determined from underlying orbital orders in strongly correlated electron systems. Lattice distortions and orbital polarizations are also frequently influenced by magnetic structures. These entanglements and interplays open a possibility of controlling transport, optical and magnetic properties by various external control parameters like magnetic fields, electric fields, light, pressure etc. From this motivation, rich magnetic and orbital phases, their phase transitions and interplays have attracted much interest in strongly correlated electron systems, particularly in transition metal (TM) oxides. Cuprate superconductors and manganese perovskite compounds with colossal magnetoresistance belong to the TM oxides with $3d$ e_g bands at the Fermi level. Perovskite-type Ti oxides $RTiO_3$ with R being a rare-earth ion belong to the same type but with $3d$ t_{2g} bands at the Fermi level and show a very different behavior. Particularly, while the above mother materials are commonly typical Mott insulators, $RTiO_3$ shows markedly rich and complicated behaviors possibly due to the above interplay. The crystal structure of $RTiO_3$ is a pseudocubic perovskite with an orthorhombic distortion ($GdFeO_3$-type distortion) and exhibits a magnetic phase transition as a function of the magnitude of this distortion. $LaTiO_3$ has relatively small $GdFeO_3$-type distortion and shows AFM(G)-type magnetic structure below 130 K. The origin of this G-type antiferromagnetism has long been

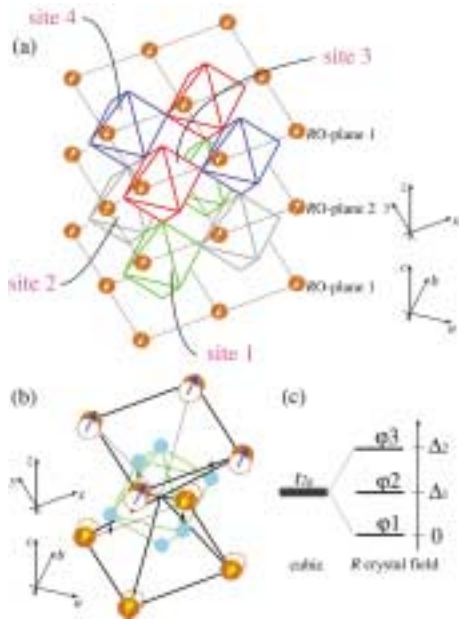

Fig. 1. (a) Displacements of the R ions along the b-axis due to the $GdFeO_3$-type distortion. In RO-plane 1, they shift in the positive direction while in RO-plane 2, they shift in the negative direction. (b) In the case of site 1, the distances between the Ti ion and R ions located in the (1,1,-1)-directions decreases. As a result, the La ions generate the crystal field which is similar to the trigonal crystal field with [1,1,-1] axis. Displacements of the O ions along the *c*-axis which are induced by the tilting of the octahedron are also presented. (c) Energy-level structure in the crystal field due to the R ions. The threefold degeneracy of the cubic-t_{2g} levels split into three nondegenerate levels.

puzzling and controversial, because naively the orbital degeneracy leads to the ferromagnetic ground state. To fully understand electron correlation effects in perovskite compounds and in more general, in *d*-electron systems, it is recognized that puzzling properties of Ti perovskites have to be explained by a convincing theory. The Ti perovskite compound also offers touchstone materials for the understanding of orbital physics, which is a hot topic of the physics of electron correlation.

In our study it has turned out that a very simple mechanism of the R crystal field resulted from the displacement of R ion caused by the well-known $GdFeO_3$-type distortion leads to a consistent picture for the experimental results. We have examined the crystal field of La cations by considering the experimentally observed distortion of the La ions. The crystal field Hamiltonian is constructed by using the experimental position parameters. Based on this Hamiltonian, we have shown that the distortion of the La ions caused by the $GdFeO_3$-type distortion generates the crystal field with lower symmetry, which is similar to the trigonal crystal field. Then the threefold degenerate cubic-t_{2g} levels split into three isolated levels. The energies and the spin-exchange constant calculated by the effective Hamiltonian show that the lowest-level occupations in this crystal field stabilize the AFM(G) state (see Fig. 1). Since the perovskite titanates attract an enormous amount of interest, a number of experiments have been done so far. However, there had been no theory which can explain these experimental results in a unified way. Now the following experimental results are explained within our theory [1,2].

(1): Emergence of the antiferromagnetic(G) (AFM(G)) states.

We have shown that the AFM(G) state is realized with quenched orbital degrees of freedom due to the crystal field from R ions.

(2): Neutron scattering [3]

Recent neutron scattering experiment showed the spin-wave spectrum characterized by isotropic spin couplings as well as a small spin gap for $LaTiO_3$. These characteristics are well reproduced in our picture. The isotropic spin coupling is caused by the isotropy of transfer amplitudes in our theory.

(3): Behavior of the Néel temperature in the magnetic phase diagram.

According to the experimentally obtained magnetic phase diagram [4], the Néel temperature monotonically decreases as R goes from La, Pr, Nd to Sm with increasing $GdFeO_3$-type distortion. The calculation of the spin coupling based on our theory well reproduces this behavior.

(4): Resonant x-ray scattering.

Recent resonant x-ray scattering experiment showed the evidence of an orbital ordering in the AFM(G) compounds of $RTiO_3$ (R=La, Pr, Nd and Sm) and that the symmetry of the orbital ordering is the same as that in the FM compounds $YTiO_3$ and $GdTiO_3$ [5]. Our present calculation of the orbital state based on our theory well explains this result.

(5): X-ray diffraction measurement.

We have shown that the crystal fields from La cations stabilize an orbital ordering in which (*xy*-*yz*-*zx*), (*xy*-*yz*-*zx*), (*xy*+*yz*+*zx*) and (*xy*+*yz*+*zx*) are approximately occupied at four Ti sites in the orthorhombic unit cell. This orbital ordering is expected to induce nearly trigonal distortions of TiO_6 octahedra. These distortions were actually observed by recent x-ray diffraction measurements [6,7].

(6): NMR

A NMR spectrum for $LaTiO_3$ can be well reproduced if we take an orbital ordering model predicted in our theory [8].

Through this study, it has clarified that in the perovskite type transition-metal oxides, a crystal field from the R ions caused by the $GdFeO_3$-type structure lifts the 3*d* orbital degeneracy. This mechanism of lifting the orbital degeneracy competes with the usual Jahn-Teller mechanism, and eventually plays an important role in controlling the orbital-spin structures. The finding of this mechanism is of fair and general importance since the $GdFeO_3$-type distortion is a universal phenomenon, which is seen in a large number of perovskite-type compounds. This mechanism may also play important roles on the electronic structures in other perovskite compounds.

References

[1] M. Mochizuki and M. Imada, J. Phys. Soc. Jpn. **70**, 2872-2875 (2001).
[2] M. Mochizuki and M. Imada, cond-mat/0301049
[3] B. Keimer, D. Casa, A. Ivanov, J. W. Lynn, M. v. Zimmermann, J. P. Hill, D. Gibbs, Y. Taguchi and Y. Tokura, Phys. Rev. Lett. **85**, 3946 (2000).
[4] T. Katsufuji, Y. Taguchi and Y. Tokura, Phys. Rev. B **56**, 10145 (1997).
[5] M. Kubota, H. Nakao, Y. Murakami, Y. Taguchi, Y. Tokura, M. v. Zimmermann, J. P. Hill and D. Gibbs: unpublished.
[6] M. Cwik, *et al*., cond-mat/0302087.
[7] J. Hemberger, *et al*., cond-mat/0303070.
[8] M. Itoh, T. Kiyama *et al*., unpublished.

Authors
M. Mochizuki and M. Imada

Berry Phase and Spin Quantum Hall Effect in the Vortex State of Superfluid ^{3}He in Two Dimension

M. Kohmoto

The Berry phase arises in quantum-mechanical systems with an adiabatic change on a closed loop in a parameter space [1]. In spite of the fact that it is a phase of the wave function, it could be related to physical effects and, in some cases, has a connection with topological numbers. The quantum Hall effect in Bloch electron systems is described as an adiabatic charge transport whose process is closed in a parameter space. A Berry phase is generated and the quantized Hall conductivity is written by the Berry phase as well as the Chern number [2].

Recently, it has been pointed out that quasiparticles in the vortex lattice of $d_{x^2-y^2}$-wave superconductors are in the Bloch states [3]. The spin quantum Hall effect occurs and its conductivity is written by a Chern number [4]. Then, one can expect that the spin Hall conductivity in the vortex state is written by a Berry phase, when the effect can be described as an adiabatic spin transport of a closed process.

Here, we discuss Bloch quasiparticles in the vortex state of *p*-wave superfluid ^{3}He in two dimensions. To realize 2D, we introduce a strong confine potential along the *z* axis to avoid quasiparticle excitations along the *z* axis. The boundary effect introduced by the confine potential locks the relative angular momentum of all the Cooper pairs in the same direction along the *z* axis. Then, we take the *z* component of the angular momentum is 1 in the whole region. The direction of the *d* vector becomes parallel to the angular momentum because of the existence of the magnetic dipole interaction which couples spin and orbit.

It is well known that the rotating superfluid is direct analogy of type-II superconductors, and actually the vortex states in superfluid ^{3}He are detected by the experiments [5]. Then, we consider superfluid in a container that rotates around *z* axis. The vortex is assumed to be form a square lattice (see Fig1.). Because of the periodicity of the vortex lattice, the energy eigenstates of the quasiparticle are the Bloch states and parameterized by the momentum in the Brillouin zone.

We also consider that the system is in a magnetic field with a weak and homogeneous gradient. Such a field cannot be introduced in superconductors due to the Meissner effect. The magnetic field couples to spin through the Zeeman term and does not to orbital currents because of the neutrality of the superfluid. The magnetic field could be represented by an adiabatically changing vector potential which couples to the spin current. The adiabatic process is defined on a closed loop in the Brillouin zone, so it generates a Berry phase.

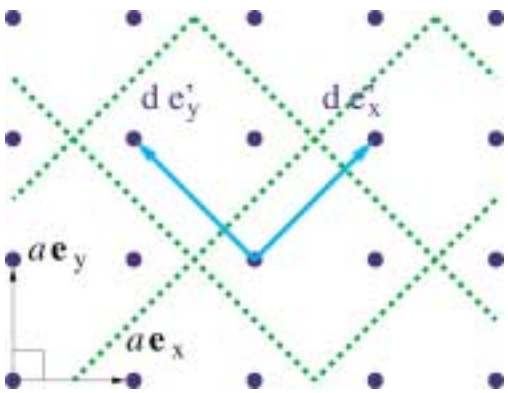

Fig. 1. A square vortex lattice. The blue dots denote the vortex cores in the lattice. The black tin arrows denote the lattice periodicity. Quantum theory admits the only symmetries which commute each other, so the wave functions of the quasiparticles are the Bloch states for the periodicity denoted by the cyan arrows.

The spin Hall current flows in the process above. We calculated the expectation value of the total spin current directly by using the adiabatic approximation and obtain the spin Hall conductivity. The conductivity is represented by the Chern number and quantized when the quasiparticle has an excitation gap as that in the *d*-wave vortex state. We have shown that the spin Hall conductivity is written by the Berry phase. The spin transfer per a cycle per the boundary of the unit cell is quantized and related to the Berry phase.

We would like to comment on the fact that, in our argument, the orbital part of the pairing symmetry is not crucial as long as the quasiparticle spectrum in the vortex state has an excitation gap. The spin part is crucial because the spin rotational symmetry is needed to obtain well-defined spin currents. Several authors have made efforts to find a way to measure spin transport [5]. Some experimental techniques to detect spin transfer are highly desirable.

References

[1] M.V.Berry, Proc. R. Soc. London. Ser. **A 392**, 45 (1984).
[2] M.Kohmoto, Ann. Phys. (N.Y.) **160**, 355 (1985).
[3] M.Franz and Z.Tesanovic, Phys. Rev. Lett. **84**, 554 (2000).
[4] O.V.Lounasmaa and E.Thuneberg, Proc. Natl. Acad. Sci. U.S.A. **96**, 7760 (1999).
[5] See, for example, J.E.Hirsch, Phys. Rev. Lett. **83**, 1834 (1999).

Principal Publication and Authors

J. Goryo[a] and M.Kohmoto, Phys. Rev. B **66**, 174503 (2002).
[a]Aoyama Gakuin University

Possibility of a Metallic Phase in the Half-Filled Hubbard-Holstein Model

Y. Takada

For the last few decades, the competition between the phonon-mediated electron-electron attraction and the local Coulomb repulsion has been discussed in various contexts of condensed matter physics. Initially the problem was raised in relation to the quasi-one dimensional organic charge-transfer salts. In recent years, it has also become an important issue in studying the perovskite oxides such as cuprates and manganites.

Theoretically the Hubbard-Holstein (HH) model serves as a useful framework to investigate the competition. In addition to the kinetic-energy term represented by *t* the nearest-neighbor electron hopping integral, it consists of two interaction parts. One is the term describing the electron correlation effects through *U* the on-site Coulomb repulsion as in the Hubbard model. The other is the term to couple an electron with local phonons as in the Holstein model, leading to $\alpha\omega_0$ the polaron stabilization energy with α the non-dimensional electron-phonon coupling constant and ω_0 the optic phonon energy.

For this model, there have already been many previous works using various methods. These studies have revealed that the HH model can afford interesting phase diagrams due to the competition among charge-density wave (CDW), spin-density wave (SDW), and superconductivity as we change the parameters involved in the system, *i.e.*, *U*, α, *t*, ω_0, and *n* the electron filling. Roughly speaking, the CDW

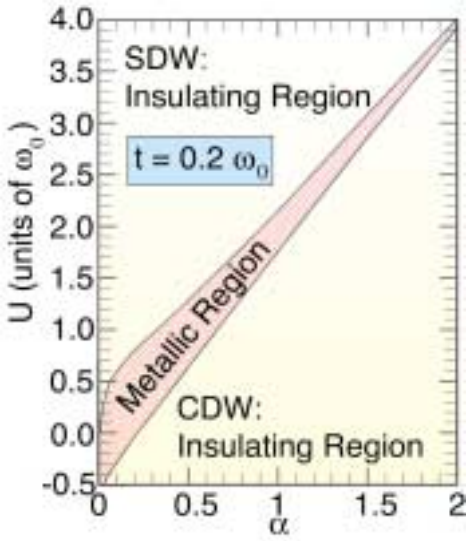

Fig. 1. Phase diagram in the (α,U) plane for the half-filled Hubbard-Holstein model.

(SDW) nature manifests itself in the ground state at half filling (n=1), if the effective electron-electron interaction $U_{\rm eff}$ (~ U-2$\alpha\omega_0$) is negative (positive).

However, the detail of the CDW-SDW transition is not known well. In fact, the appearance of a superconducting phase is suggested [1] in the exact-diagonalization study on the two-site HH model. Thus we carefully consider the transition region at half-filling by approaching the HH model from the antiadiabatic region (t«ω_0) where the variable displacement Lang-Firsov canonical transformation is useful. In order to avoid any error that might enter through the approximations involved in dealing with the Coulomb correlation term, we have investigated the one-dimensional system so that the exact solution of Lieb and Wu can be taken advantage of. By determining the displacement variationally, we have obtained fairly accurate results for the properties of the ground state. [2]

In Fig. 1, we show the obtained phase diagram in the (α,U) plane at t=0.2ω_0. The metallic phase characterized by the local spin moment L_0~3/8 and a small effective mass of

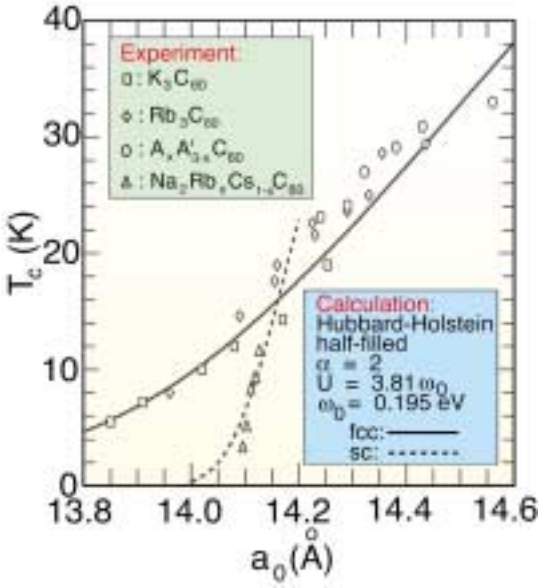

Fig. 2. Superconducting T_c as a function of the lattice constant a_0 in A_3C_{60} and its dependence on the crystal structure in comparison with experimental results.

polarons appears along the line of U=2$\alpha\omega_0$, namely, in the CDW-SDW crossover region. This phase seems to continuously convert into the superconducting phase in the attractive Hubbard model (or the system with α=0 and U<0).

We do not believe that this behavior is specific to one dimension (1D); a similar metallic behavior will be seen in higher dimensions as well, as long as $|U_{\rm eff}|$ is less than the polaron bandwidth in the crossover region. We may even conjecture that such a metallic phase will be realized more easily in higher dimensions in which we can avoid unusual phenomena specific to 1D like the Mott transition at U=0 irrespective of t in the 1D Hubbard model.

It is not known for sure whether this kind of a metallic phase has already been observed in actual materials or not, but it has been pointed out [3,4] that physical properties including superconductivity in the alkali-doped fullerenes A_3C_{60} can be reproduced in a unified way in terms of this picture. For example, the superconducting transition temperature T_c in the HH model with suitably chosen parameters is obtained as a function of the lattice constant a_0 as shown in Fig. 2.

References

[1] Y. Takada, J. Phys. Soc. Jpn. **65**, 1544 (1996).
[2] Y. Takada and A. Chatterjee, Phys. Rev. B **67**, 081102(R) (2003).
[3] Y. Takada, J. Phys. Soc. Jpn. **65**, 3134 (1996).
[4] Y. Takada and T. Hotta, Int. J. of Mod. Phys. B **12**, 3042 (1998).

Authors
Y. Takada and A. Chatterjee[a]
[a]University of Hyderabad.

Aharonov-Bohm-Type Oscillations in Triangular Antidot Lattice

Y. Iye

High mobility two-dimensional electron gas (2DEG) at GaAs/AlGaAs heterointerface provides an ideal stage to explore various quantum transport phenomena in controlled environment. Use of microfabrication techniques allows us to prepare a variety of artificial structures in mesoscopic scale. Antidot lattice is one of such artificial structures in which high potential regions (andidot) for the 2DEGs are periodically arranged to constitute a lateral superlattice as shown in Fig.1.

The right panel of Fig.1 shows a potential landscape and a scanning electron micrograph of a triangular antidot lattice. For this sample, the lattice period is a=960 nm and the diameter of the antidot is d=576 nm.

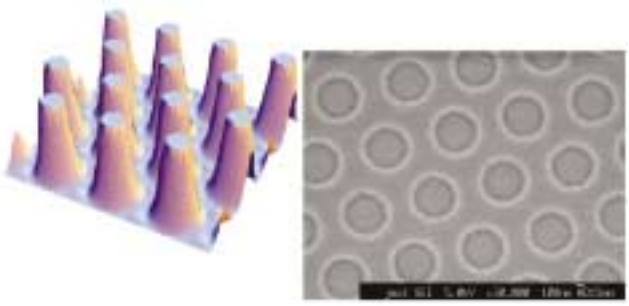

Fig.1. *Left*: Potential landscape of a triangular antidot lattice. *Right*: Electron micrograph of a sample used in this study.

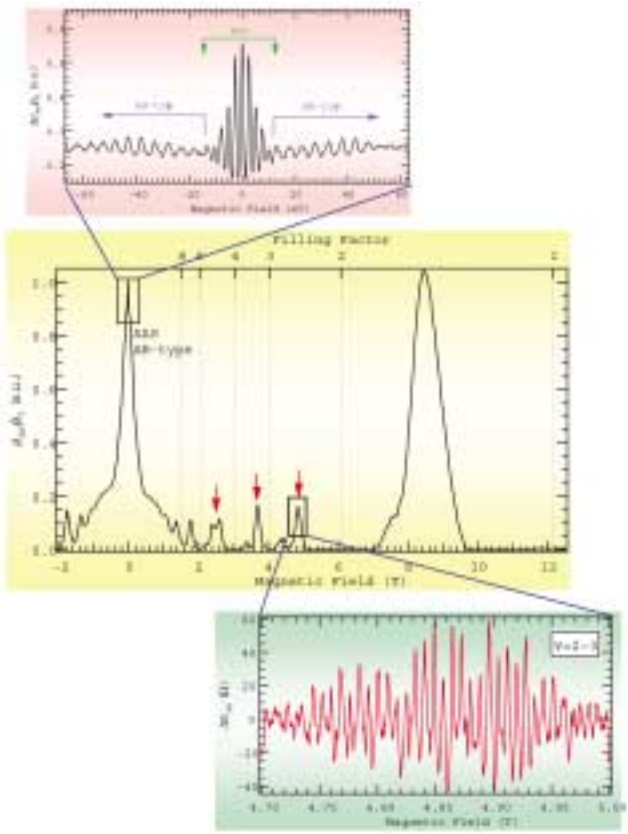

Fig. 2. *Main Panel*: Magnetoresistance of a triangular antidot lattice. *Top panel*: Oscillatory part of the resistance near zero magnetic field. The AAS(*h*/2*e*) and AB-type (*h*/*e*) oscillations are identified. *Bottom panel*: oscillatory part of resistance at around the peak between the ν=3 and 2.

The main panel of Fig.2 shows a magnetoresistance trace of the triangular antidot lattice sample measured at 30 mK. Three types of oscillations have been observed. At low magnetic field, the so-called Altshuler-Aronov-Spivak (AAS) oscillation with *h*/2*e* period and the Aharonov-Bohm (AB)-type oscillation with *h*/*e* period are observed on top of a large negative magnetoresistance. The top panel shows the oscillatory part of resistance in this region. The periods of these oscillations agree with those expected from to the unit cell area.

In the quantum Hall regime at higher magnetic field, another series of AB-type oscillations with periods longer than the low-field counterpart are observed as shown on the bottom panel of Fig.2. The periods of the high field AB-type oscillations reflect the area of edge state encircling each antidot.

The AB-type oscillation is different in nature from the ordinary AB oscillation in a single ring, which is known to diminish upon ensemble averaging. The AB-type oscillation in antidot lattice observed in a macroscopic sample much larger than the decoherence length is attributed to oscillatory fine structures of the density of states, which arises from unstable periodic orbits inherent to the chaotic system.

The temperature dependence of the amplitude of oscillations reveals characteristic decoherence mechanisms, which are different among the these oscillatory phenomena and from those found in the single ring case.

Authors
M.Ueki, T.Terada, A.Endo, S.Katsumoto, Y.Iye

What Causes Quantum Decoherence in Mesoscopic Circuits?

S. Katsumoto

Quantum decoherence, which separates quantum mechanics and classical one, has been a most important issue in physics since the establishment of quantum mechanics. Quantum transport in mesoscopic systems is one of the best laboratories of the decoherence. Here we present a possible mechanism of decoherence, *i.e.*, spin-states in quantum dots.

A quantum dot (QD) and an Aharonov-Bohm (AB) ring are two extremes of quantum devices. The former emphasizes the particle nature of electrons through the single-electron charging effect, while the latter highlights them as waves through the interference. We showed that in a QD-AB ring composite system such as shown in Fig.1(a), both characteristics of electrons emerge as the Fano effect [1].

Then does no decoherence occur in such composite systems? A possible mechanism is illustrated in Fig.1(c). When the top electronic state is half-occupied with an electron, say with up-spin, an electron with down spin can come into the dot. But the outgoing electron can be either with up-spin or down-spin. If it is with up-spin, this cannot interfere with the other part traversed through the "reference arm" part of the ring, thus results in decoherence.

If this mechanism emerges, the coherence of the total system should be largely affected by the number of electrons. That is, when the number is even, the top level should be empty in the simplest model and there is no decoherence, while half of traversing electrons cannot interfere when the number is odd. The number of electrons in a quantum dot changes by one just at the peaks of Coulomb oscillation. The amplitude of AB oscillation is a good measure of quantum coherence. Hence the above inference leads to the prediction that the AB amplitude should be largely changed when the gate voltage crosses peaks of Coulomb oscillation.

Figure 2 shows a result of measurement at a Coulomb peak. As shown in the lower panel, the AB amplitude, thus the quantum coherence is larger at the left side of this Coulomb peak. Steep decrease and "lapse" of AB phase at

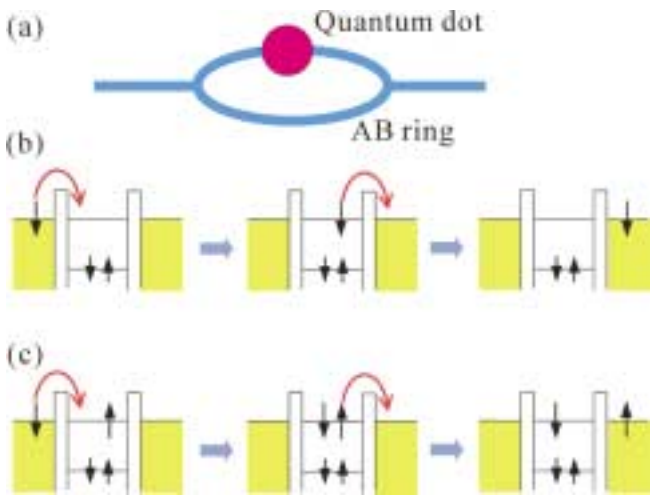

Fig. 1. (a) Schematic diagram of the sample circuit. (b) When the top "spin-pair" state is empty, an electron tunnels through the dot without spin-flip. (c) When the top state is half-occupied, spin-flip process which causes decoherence is possible.

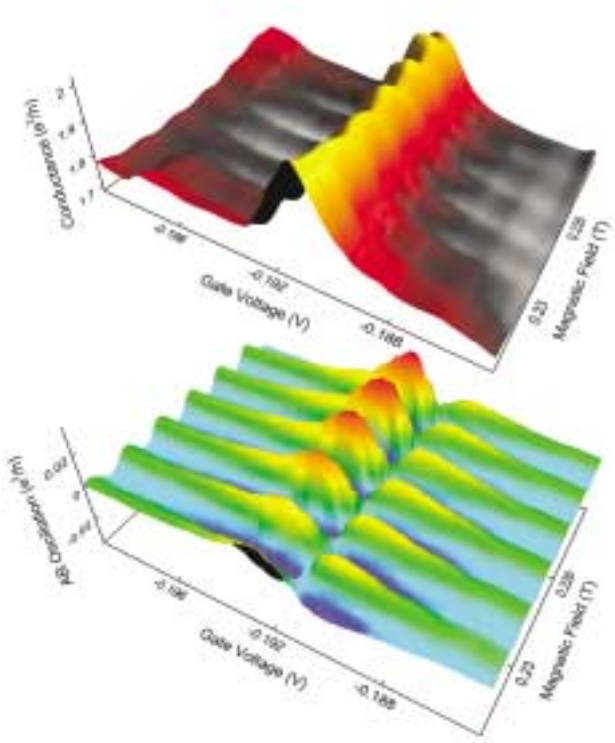

Fig. 2. Upper panel: 3D plot of conductance versus a plane of gate voltage and magnetic field across a Coulomb peak. Small oscillation against the magnetic field is AB oscillation. Lower panel: Extracted AB component. Apparently the AB amplitude is larger in the left side of the Coulomb peak. Phase lapse of π is also seen at the peak.

the peak is due to the two-terminal nature of the device. This asymmetry is reduced by comparatively high (-2 T) magnetic field due to the Zeeman splitting.

These features agree with the theoretical prediction and we believe the observed asymmetry is due to the above described decoherence mechanism. What happens then, when such spin-flip scattering makes up coherent Kondo states? That would be a most important issue in our research.

Reference

[1] K. Kobayashi, H. Aikawa, S. Katsumoto and Y. Iye, Phys. Rev. Lett. **88**, 256806 (2002).

Authors
K. Kobayashi, H. Aikawa, A. Sano, S. Katsumoto and Y. Iye

Novel One-Dimensional Nanopatterns on Vicinal Cu(001)-c(2×2)N Surfaces

F. Komori

Self-organization of adsorbate-induced domains on solid surfaces has been one of the important subjects of nanoscale science. It has been shown that one- and two-dimensional nanopatterns can be made on surfaces by adjusting the coverage of adsorbates and adsorption temperature. On a nitrogen-covered Cu(001) surface, there forms a grid pattern consisting of $c(2\times2)$N square patches of 5×5 nm^2 and 2 nm wide clean Cu surface at half monoatomic layer coverage [1] as shown in Fig. 1(a). The surface was prepared by annealing a Cu(001) crystal to about 670 K in 5 min after

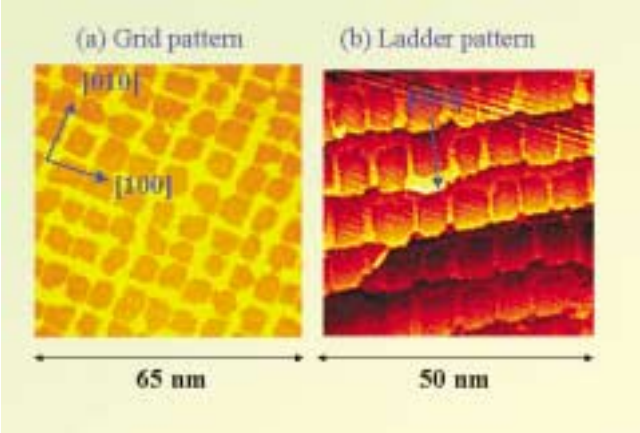

Fig. 1. (a) A square grid pattern of 7 nm period on a flat nitrogen-adsorbed Cu(001) surface. Clean Cu surface is imaged bright and $c(2\times2)$N surface dark. Nitrogen density in this image is 1/4 of Cu surface atoms density on average. Sides of the square $c(2\times2)$ patches are along ⟨100⟩ directions. (b) One dimensional array of the square $c(2\times2)$N patches on a N-adsorbed Cu(001) surface vicinal to [010] direction. Width of the terrace is quantized by the period of the grid pattern. Formation of these patterns is attributed to strain-relief on clean Cu surface and monoatomic steps.

the nitrogen ion irradiation on the surface at room temperature. This pattern formation is mainly attributed to the relaxation of the elastic strain due to the lattice expansion on the nitrogen-adsorbed surface. Here, the clean Cu surface and the monoatomic steps act as strain relievers although the role of the step is secondary for the formation of the grid pattern.

We have found that step density and direction drastically influence the formation of one-dimensional patterns on Cu(001)-$c(2\times2)$N vicinal surfaces [2]. Figure 1(b) shows one-dimensional array of the N-adsorbed square patches on the surface vicinal to the [100] direction. In this case, the width of the terrace is fixed to the period of the grid pattern. On the surface vicinal to the [-110] direction, on the other hand, a labyrinth pattern is formed as shown in Fig. 2(a). Here, the lines of clean Cu surface are aligned along the

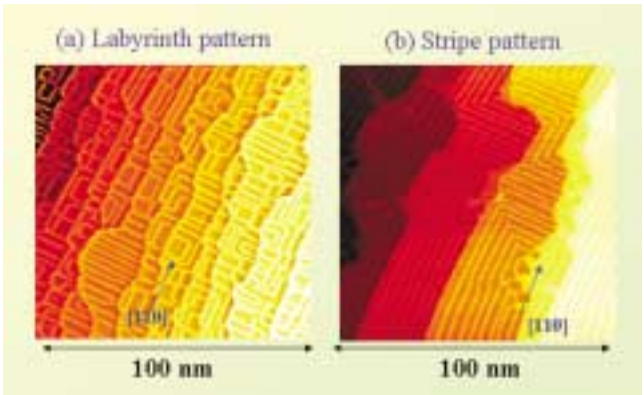

Fig. 2. (a) A labyrinth pattern formed on a nitrogen-adsorbed Cu(001) surface vicinal to [-110]direction. The lines of clean Cu surface of 1-2 nm wide are along the ⟨110⟩ directions, and the size and shape of the N-covered domains are inhomogeneous. (b) A stripe pattern on a nitrogen-adsorbed Cu(001) surface vicinal to [-110] direction. This pattern was obtained by annealing the surface in Fig. 2(a). The width of N- adsorbed stripe domain parallel to the [-110] direction is smaller than that parallel to the [110] direction. Small areas with the square $c(2\times2)$N patches coexist.

⟨110⟩ direction. The size and shape of the nitrogen-covered domains are inhomogeneous on the surface. The image in Fig. 2(b) shows the result of subsequent annealing of the sample in Fig. 2(a) for 5 min. The stripe domains parallel to the [110] direction occupy three times larger area than the domains with the stripe parallel to the [-110] direction, and small areas with the square patches coexist. We notice that there are short strips of clean Cu surface along ⟨100⟩ directions at the corners of two long clean Cu lines along ⟨110⟩ directions.

Main characteristics of the stripe patterns can be explained by assuming an anisotropic expansion of the lattice at $c(2\times2)$N surface; the lattice constant increases only along the direction perpendicular to the clean Cu lines while that along the Cu line remains the same. No strain reliever is necessary in the direction of the Cu lines while both the step edges and the clean Cu surface are the relievers in the perpendicular direction. The observed short strips of clean Cu surface end at the centers of the $c(2\times2)$ stripe domain, and never connect two clean Cu lines. In the present model, the short strips are formed only highly compressed surface at the corners consistently with the general formation mechanism of the clean Cu lines.

References
[1] F.M. Leibsle, C.F.J. Flipse and A.W. Robinson, Phys. Rev. B **47**, 15865 (1993).
[2] S. Ohno, K. Yagyuu, K. Nakatsuji and F. Komori, Jpn. J. Appl. Phys. **41**, L1243 (2002).

Authors
S. Ohno, M. Yamada, K. Yagyuu, K. Nakatsuji and F. Komori

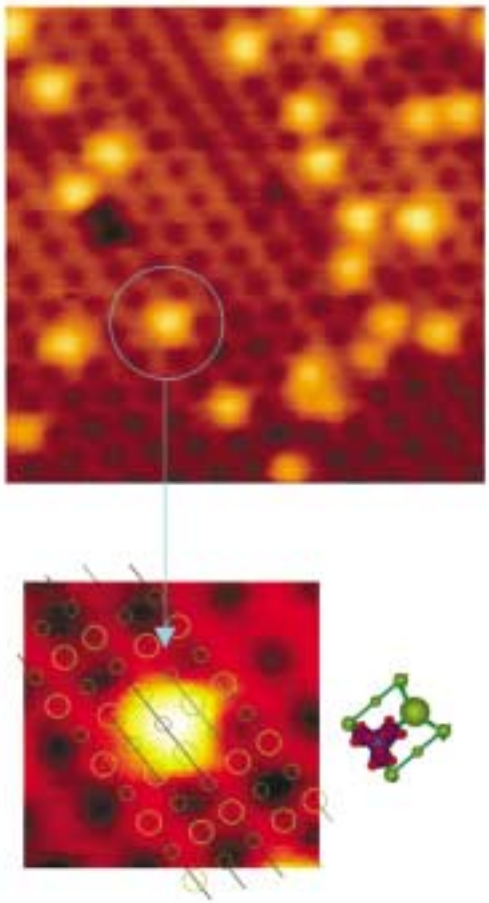

Fig. 1. Occupied state STM images of the Si(100)$c(4\times2)$ surface exposed to TMA at 80 K. V(sample) = -2.2 V, I = 0.1 nA. The schematic adsorption model is also shown.

Site-Specific Reactions of the Buckled Dimer on Si(100)c(4×2) at Low Temperature

J. Yoshinobu

The Si(100) surface is reconstructed to form a (2×1) dimer row structure. Many experimental and theoretical studies have supported the buckled (asymmetric) dimer with the $c(4\times2)$ phase as a ground state. One of the fundamental interests on Si(100) is how the spatial localization of electron density of surface atoms controls the reactivity towards different molecules. In the buckled dimer on Si(100)$c(4\times2)$, a partial charge transfer occurs from a down dimer atom (Sd) to an up dimer atom (Su) and thus the Su and Sd atoms become partially negatively and positively charged, respectively. Hence, the reactivity of the Su and Sd atoms is expected to be highly selective towards Lewis-acid and Lewis-base molecules. We studied the adsorption of trimethylamine TMA and water molecules on Si(100)$c(4\times2)$ using low temperature STM.

TMA on Si(100)c(4×2) at 80 K

Trimethylamine (TMA) being a typical Lewis base molecule has drown much attention to study the fundamental of Lewis base-silicon surface interaction. In spite of several studies on this system, there is no direct experimental evidence about the site-specific adsorption of adsorbed TMA on Si(100).

In Figures 1, many bright protrusions are observed for the TMA adsorption on Si(100)$c(4\times2)$ at 80 K. The protrusions are randomly distributed on the surface. All the bright protrusions are located at either side of the center of dimer row and most of the protrusions are triangle-shaped. One of the three corners of triangle shape protrusion is pointed towards the dimer bond direction, and the center of the triangle-shaped protrusion is located on the down atom. We have ascribed the triangle shaped protrusion due to the three methyl groups in the adsorbed TMA. Thus, the location and shape of protrusion clearly indicates that the molecular adsorption of TMA is purely site-specific on the down dimer atom.

Water on Si(100) : C-type defect

Defects on the surface play a crucial role not only in chemical reaction, thin film growth but also electronic properties at the surface and interface. One of the long-standing unsettled problems in surface science is the origin and atomic structure of *C*-defects commonly observed on the Si(100) surface. The number of *C*-defects was increased by the water exposure on Si(100) at both room and low temperature.

At 80 K, the *C*-defect appears as an asymmetric teardrop shaped protrusion in the high-resolution unoccupied state image as shown in Fig. 2. The protrusions are marked by U, U′, D, and D′ depending on its position and direction of the asymmetry. The U and U′ (D and D′) are the mirror image of each other (enantiomorphic) where the mirror plane is perpendicular to the dimer row. The U and D (U′ and D′) are also enantiomorphic where the mirror plane is parallel to the dimer row. Different orientation of *C*-defects is also observed in the occupied state image at 80 K. By virtue of

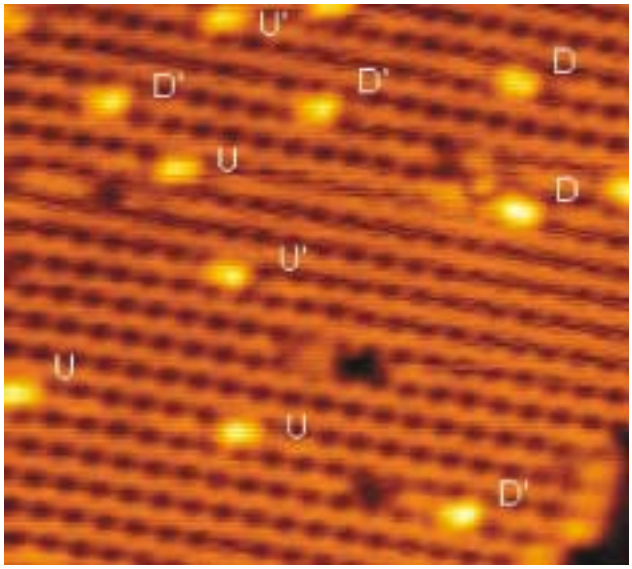

Fig. 2. Unoccupied state STM image of Si(100)c(4×2) at 80 K. V(sample) = 1.0 V, I = 0.1 nA The asymmetric teardrop shaped protrusions are C-defects. The protrusions are marked by U, U′, D and D′ depending on its position and the direction of asymmetry.

the alternate buckled dimer arrangement on Si(100)c(4×2) at low temperature (<200 K), the registry of C-defect is clearly identified, i.e. the 'head' and 'tail' of the asymmetric protrusion lie on down dimer atom and the up dimer atom of the adjacent dimer, respectively. The results unambiguously indicate that the C-defect is caused by the dissociative adsorption of single water molecule on the same side of two adjacent dimers.

Authors
M.Z. Hossain, Y. Yamashita, K. Mukai and J. Yoshinobu

Dimer Buckling of the Si(001)2×1 Surface Observed by Low-Temperature Scanning Tunneling Microscope

Y. Hasegawa

On the Si(001)2×1 surface, a dimer structure is formed for a reduction of the dangling bond. The unique feature which leads the surface to show a variety of phases is buckling of the dimer: the two dimer-composing atoms are located up and down. According to the generally accepted scenario on a temperature dependence of the structure, an order-disorder phase transition occurs around 200 K; below the temperature the buckled dimers are arranged with the c(4×2) ordering, and above the temperature the thermally activated dimer flip-flop motion breaks the symmetry to exhibit the 2×1 ordering. Recently, Kondo et al. [1] and Yokoyama and Takayanagi [2], however, reported STM images taken below the transition temperature showing symmetric dimers. Their results are inconsistent with the above scenario, casting a doubt on the accepted ground state structure.

It has been argued that uncertainty of sample temperature could be the origin of the inconsistent observations. To avoid the uncertainty, we first measured the temperature with a resistance sensor attached on a dummy sample, and

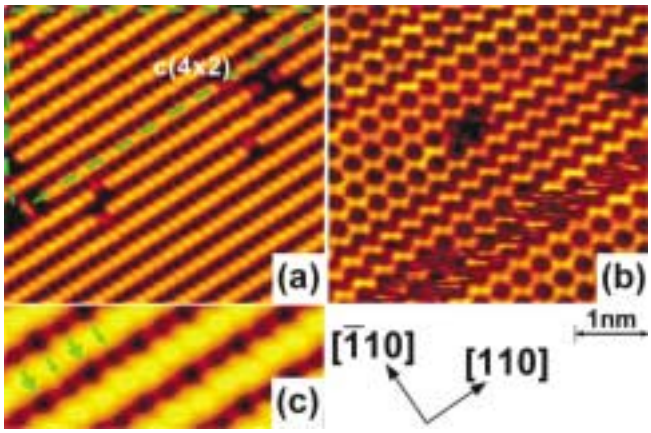

Fig. 1. STM images taken below 10K with a sample bias voltage of -2.2 V (a) and +1.6 V (b). The filled state image (a) apparently shows symmetric dimers while the empty state image (b) shows buckled dimers. In an area surrounded by a dashed green line in image (a) (zoomed in (c)) a faint trace of the c(4×2) structure; alternative array of dark spots between the dimer rows, are observed, indicating an existence of the c(4×2) periodicity and the buckled dimers there.

confirmed that the sample temperature during our observation is below 10 K [4].

Figure 1 shows STM images taken at 10 K. In the filled state image (Fig. 1(a)) most of the surface area is seemingly covered with symmetric dimers. In fact, however, for instance in the zoomed area shown in Fig. 1(c), a very faint pattern of alternative dark spots between the dimer rows is found. The pattern, with a periodicity of the c(4×2) structure, must be a trace of the intrinsic c(4×2) structure overlapped with the symmetric-dimer appearance. We believe that this is an evidence of the dimer buckling at this temperature. In the empty state image, presented in Fig. 1(b), almost all area is filled with zigzag dimer rows, supporting for an presence of buckled dimers.

Apparent symmetric dimer imaging is observed only at low temperature (<10 K). At an elevated temperature only buckled dimers were observed in both polarities of the bias voltage. We found that transition temperature between the symmetric and buckled dimer imaging in filled state images is around 40 K for the sample we used. It has been known that in silicon the carrier concentration drops dramatically around 40 K. Since in the filled state STM observation holes are inherently injected, we speculate that the apparent symmetric imaging is related with the reduced screening effect to the injected charges. As a result of the charging, potential at the surface is locally lowered, presumably making possible for the electrons in the π^* states to be probed in the condition of the filled state imaging.

References

[1] Y. Kondo, T. Amakusa, M. Iwatsuki, and H. Tokumoto, Surf. Sci. **453**, L318 (2000).
[2] T. Yokoyama and K. Takayanagi, Phys. Rev. B **61**, R5078 (2000).
[3] S. B. Healy, C. Filippi, P. Kratzer, E. Penev, and M. Scheffer, Phys. Rev. Lett. **87**, 016105 (2001).
[4] M. Ono, A. Kamoshida, N. Matsuura, E. Ishikawa, T. Eguchi, and Y. Hasegawa, Phys. Rev. B **67**, R201316 (2003).

Authors
M. Ono, A. Kamoshida, N. Matsuura, E. Ishikawa, T. Eguchi, and Y. Hasegawa

Tuning the In-Plane Lattice Constant of an Oxide Substrate

M. Lippmaa

The properties of thin heteroepitaxial oxide films often deviate significantly from the properties of bulk crystals with the same composition. The most common reason for this is the presence of lattice strain in thin films, caused by a mismatch in lattice constants of the film and a single-crystal substrate. Systematic studies of the effects of lattice strain are complicated by the very limited choice of high-quality substrates available for thin film growth. The only practical way of generating small strains in oxide lattices is to use a strain-control buffer layer. Traditional buffer layer design relies on the gradual relaxation of a lattice constant in a mismatched heteroepitaxial layer. Residual strain can then be tuned by adjusting the buffer layer thickness. This method has a number of drawbacks, mainly because the final strain depends on a variety of process parameters, such as growth rate, temperature, etc.

In order to avoid such problems, we have developed a bilayer buffer for tuning the in-plane lattice constant of a substrate. The final in-plane lattice constant on the buffer surface depends only on the composition, which is easy to control and is not sensitive to precise processing parameters.

We start by growing a thin $BaTiO_3$ layer on a $SrTiO_3$ substrate at a relatively low temperature of 650 °C. The layer thickness can be 10 nm or less. A much thicker layer of $Ba_{1-x}Sr_xTiO_3$ is then grown on top of the $BaTiO_3$ layer at the same temperature. The films grow in a layer-by-layer mode and contain, as expected, a large number of dislocations (Fig. 1(a)). Annealing the film at up to 1350 °C for 30 minutes allows the defects to migrate in the crystal. As shown in a post anneal TEM image in Fig. 1(b), all the defects migrate either to the highest mismatch $SrTiO_3$/$BaTiO_3$ interface, or to the film surface. No defects could be found in TEM images of the annealed film. The final lattice constant of the buffer is determined only by the Sr content of the $Ba_{1-x}Sr_xTiO_3$ layer and can be freely tuned in the 0.39 to 0.40 nm range, a span of 2.5%. The top part of the buffer is also fully relaxed and has a step-and-terrace surface structure.

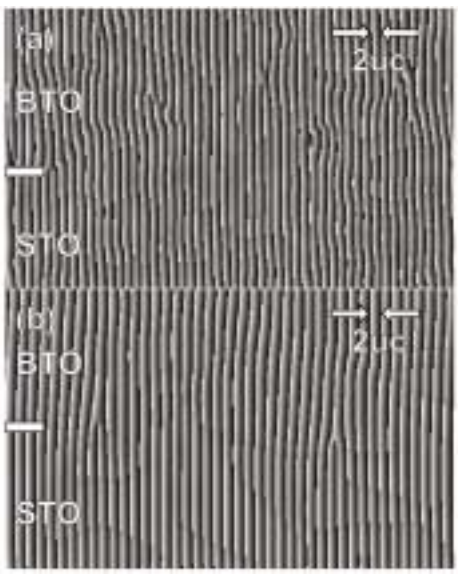

Fig. 1. Moire images generated from high-resolution cross-sectional transmission electron microscope images, showing the locations of defects in $BaTiO_3$ films grown on $SrTiO_3$. (a) A film grown at 650 °C has many defects. (b) All defects migrate to the film/substrate interface after annealing the sample at 1100 °C.

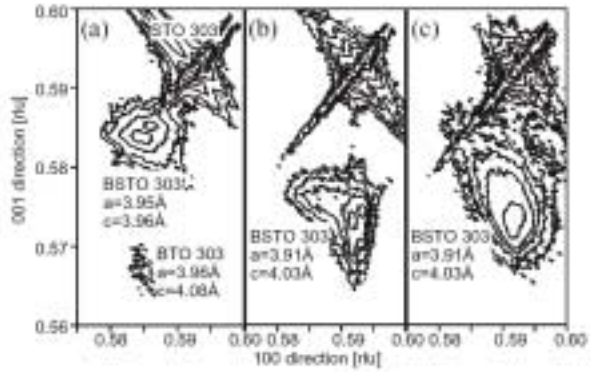

Fig. 2. Reciprocal space mapping of (a) a $Ba_{0.5}Sr_{0.5}TiO_3$ film on a $BaTiO_3$ buffer layer, (b) a $Ba_{0.5}Sr_{0.5}TiO_3$ film grown directly on a $SrTiO_3$ surface at 650 °C, and (c) partial relaxation of the same film after high-temperature annealing.

ture.

The importance of inserting a thin highly mismatched $BaTiO_3$ layer between the main buffer and the substrate can be seen in Fig. 2. The reciprocal space map in Fig. 2(a) clearly shows that the $Ba_{1-x}Sr_xTiO_3$ layer is relaxed and that the in-plane lattice constant of the thin $BaTiO_3$ layer is determined by the top part of the bilayer buffer. If the $BaTiO_3$ layer is omitted and a $Ba_{1-x}Sr_xTiO_3$ film is grown directly on a $SrTiO_3$ surface, partial lattice constant relaxation occurs, as shown in Fig. 2(b). High-temperature annealing does not improve the buffer quality (Fig. 2(c)). The presence of a highly mismatched layer is thus crucial for trapping strain-relieving dislocations at the substrate interface.

Reference

[1] K. Terai, M. Lippmaa, P. Ahmet, T. Chikyow, T. Fujii, H. Koinuma, M. Kawasaki, Appl. Phys. Lett. **80**, 4437 (2002).

Authors
K. Terai [a], M. Lippmaa, T. Ohnishi
[a] Spring-8.

Novel Magnetotransport Phenomena in Low-Dimensional Bloch Electron Systems under Strong Magnetic Fields

T. Osada

(1) Harper Broadening under Megagauss Fields

The RF technique for transport measurement has been developed under pulsed ultra-high magnetic fields generated by the single-turn coil device (B<120 T) and the electromagnetic flux compression device (B<300 T). Using these technique and devices, we have successfully measured the magnetoresistance of a quasi-one-dimensional (Q1D) conductor $NbSe_3$ up to 300 T. In the low temperature phase of $NbSe_3$, there remains only one small closed Fermi surface as a result of band reconstruction due to two independent CDW transitions. This small Fermi pocket causes the Shubnikov-de Haas (SdH) oscillations below ~50 T. In the magnetic quantum limit above ~50 T, where only the lowest Landau subband is occupied, magnetoresistance has a broad peak around 65 T, and decreases monotonously above it, and finally returns to the level of zero-field resistance (Fig. 1). This anomalous behavior strongly suggests the occurrence of the Harper broadening of the lowest Landau subband due

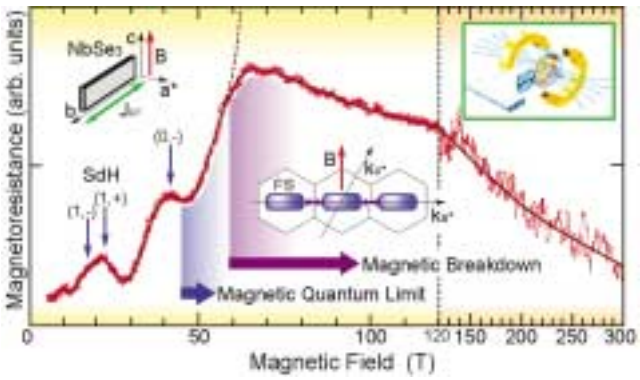

Fig. 1. Magnetoresistance of $NbSe_3$ measured by the RF transmission technique under ultra high magnetic fields up to 300 T. The data above 120 T were obtained using the electromagnetic flux compression system (inset), whereas those below 120 T were obtained using the single-turn coil system. Magnetoresistance shows monotonous decrease above 70 T, which originates from the Harper broadening of the lowest Landau subband due to magnetic breakdown.

to magnetic breakdown beyond the CDW gap.

(2) Electric Field Effect on Lebed Resonance

We have found a novel electric field effect on angular dependent magnetotransport in Q1D layered conductors with a pair of sheetlike Fermi surfaces. The Lebed resonance has known as the resonant increase of interlayer conduction at magnetic field orientations where electron orbits are periodic on Fermi sheets. Under additional interlayer electric fields, electron orbits on two Fermi sheets become periodic at different magnetic field orientations. This causes doubly splitting of the Lebed resonance of interlayer conduction. This effect provides us a new experimental tool to estimate the Fermi velocity of Q1D conductors.

We have successfully demonstrated this effect in an organic conductor α-(BEDT-TTF)$_2$KHg(SCN)$_4$. Interlayer current under strong electric fields is measured using pulse technique to avoid sample heating. As seen in the Fig.2, Lebed resonance peaks split to double peaks as the electric field is increased. From the splitting, we could estimate the Fermi velocity as 7.5×10^4 m/s.

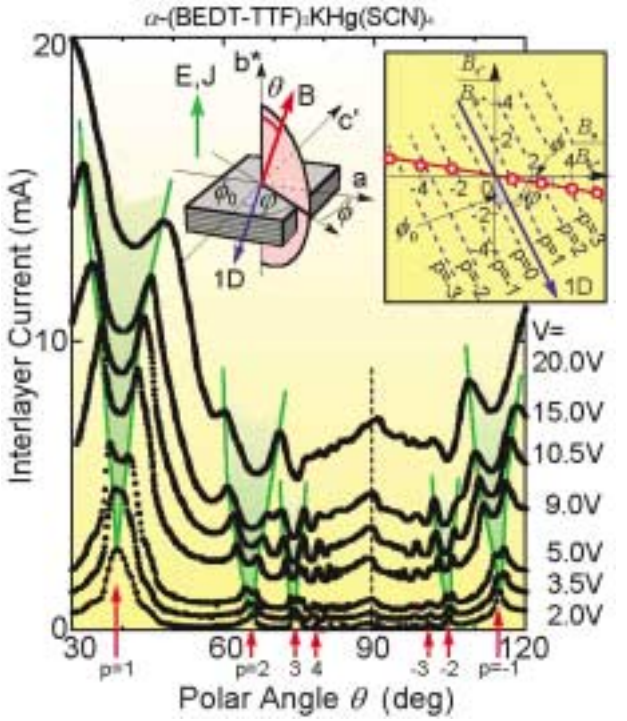

Fig. 2. Angular dependence of interlayer conduction in α-(BEDT-TTF)$_2$KHg(SCN)$_4$ under several interlayer electric fields at T=1.7 K. The magnetic field with fixed strength B=13 T is rotated in the plane normal to conducting layers with azimuth φ=54deg from the 1D axis. The Lebed resonance peaks at low electric fields indicated by red arrows split to double peaks as the electric field is increased.

Authors
T. Osada, E. Ohmichi, S. Ikeda, T. Inokuchi, K. Kobayashi, M. Kobayakawa, A. Ogasawara, and E. Komatsu

New Heavy Fermion Superconductor Ce_2CoIn_8

Y. Uwatoko

A new family of Ce based heavy fermion compounds with general formula Ce_nTIn_{3n+2} (T = Co, Rh, Ir; $n = \infty$, 1, 2) show very interesting physical phenomena such as a new type of unconventional superconductivity at ambient pressure and pressure induced superconductivity emerging upon the suppression of an antiferromagnetic order [1,2]. We have found favorable conditions for the growth of single crystal Ce_2CoIn_8. Measurements of specific heat and electrical resistivity were carried out on single crystals of Ce_2CoIn_8. The resistivity measurement reveals that Ce_2CoIn_8 is a heavy fermion superconductor with $T_c \sim 0.4$ K [3].

The specific heat divided by temperature C/T and the electrical resistivity ρ for Ce_2CoIn_8 are shown in Fig. 1. At T_c we observed a distinct jump in C/T, providing clear evidence of bulk superconductivity. However, in the C/T data we could not find any evidence for the phase transitions at T_{a1} and T_{a2} where $\rho(T)$ shows a substantial reduction. C/T of Ce_2CoIn_8 exhibits a Schottky-like peak at around 0.6 K and 2 K. The estimated value of $\Delta C/\gamma T_c \sim 0.22$ suggests very weak coupling. Here the γ value is determined to be ~ 460 mJ/K^{2}mol-Ce from the value of C/T just above T_c and ΔC is the jump in the specific heat at T_c. This ratio, of $\Delta C/\gamma T_c$, is approximately equal to that of UGe_2 in the superconducting regime at 1.15 GPa [4].

The effect of a magnetic field on the resistivity of Ce_2CoIn_8 was examined under various fixed fields up to 9 T applied parallel to the a-axis. The magnetic fields in excess of 1 T completely suppress the resistivity drop due to super-

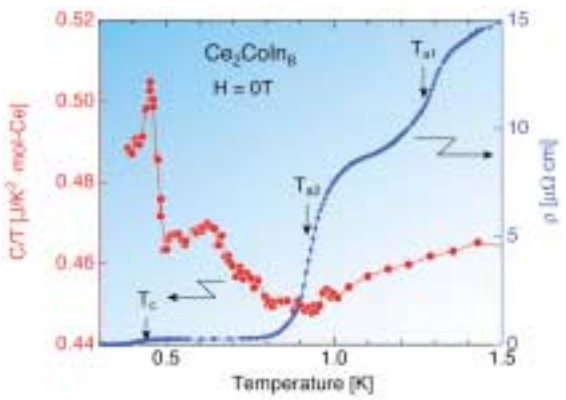

Fig. 1. Temperature dependence of the specific heat divided by temperature (red dots) and the electrical resistivity (blue dots) in the same sample of Ce_2CoIn_8. The arrows show the characteristic temperatures T_{a1}, T_{a2} and T_c determined by a peak position of the resistivity derivative $d\rho/dT$.

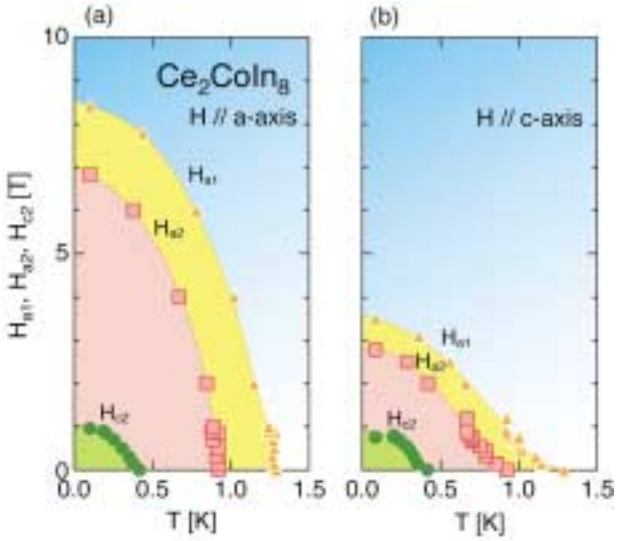

Fig. 2. Critical-field vs. temperature phase diagram for Ce_2CoIn_8 along (a) the *a*-axis and (b) the *c*-axis. Solid lines and gray mask are guides to the eyes.

conducting transition. T_{a1} and T_{a2} shifted to low temperature with increasing field. There was no structure in the resistivity at low temperature above 9 T. We have obtained the characteristic fields H_{c2}, H_{a1} and H_{a2} from the $\rho(T)$ measurements in magnetic fields applied along the *a*- and the *c*-axes. The results are plotted in Fig. 2 as a function of the temperature.

Since no anomaly is observed in C/T at T_{a1} and T_{a2}, the resistivity anomalies at these temperatures would presumably be due to the nonuniformity of the sample; e.g. stacking fault ascribable to the unique crystal structure. However, the behavior at T_{a1} and T_{a2} might also originate from the quasi-two-dimensional electronic structure peculiar to the Ce_nTIn_{3n+2} families. The problem would be settled by growing a high-quality crystals and measuring low temperature specific heat under magnetic fields.

We conclude that the transition around 0.47 K comes from intrinsic bulk superconductivity in Ce_2CoIn_8.

References

[1] C. Petrovic, P. G.Pagliuso, M. F. Hundley, R.Movshovich, J. L. Sarrao, J. D. Thompson, Z. Fisk and P.Monthoux, J. Phys. Condens. Mater **13**, L337 (2001).

[2] J. D. Thompson, R. Movshovich, Z. Fisk, F. Bouquet, N. J. Curro, R. A. Fisher, P. C. Hammel, H. Hegger, M. F. Hundley, M. Jaime, P. G. Pagliuso, C. Petrovic, N. E. Phillips and J. L. Sarrao, J. Magn. Magn. Mater **226-230**, 5 (2001).

[3] G. Chen, S. Ohara, M. Hedo, Y. Uwatoko, K. Saito, M. Sorai and I. Sakamoto, J. Phys. Soc. Jpn. **71**, 2836 (2002).

[4] N. Tateiwa, T. C. Kobayashi, K. Amaya, Y. Haga, R. Settai and Y. Onuki, Physica B **312-313**, 109 (2002).

Authors

M. Hedo, N. Kurita, Y. Uwatoko, G. Chen[a], S. Ohara[a], I. Sakamoto[a]

[a]Nagoya Institute of Technology.

Gapless Spin Liquid in the Two Dimensional Antiferromagnetic Solid ^{3}He

H. Ishimoto

Highly frustrated low-dimensional quantum antiferromagnets have attracted much attention because a magnetically disordered ground state may be realized. A low-density solid ^{3}He film adsorbed on graphite surface is one of the most ideal two-dimensional (2D) quantum spin systems with nuclear spin S= 1/2 on a triangular lattice. Because of the hard-core potential between ^{3}He atoms, the higher order multiple spin exchange (MSE) processes as well as two-particle exchange play important roles. The exchange of even number of particles is antiferromagnetic (AFM), while that of an odd ones is ferromagnetic (FM). The competition between them, in addition to the geometrical frustration inherent to a triangular lattice structure, makes the present system strongly frustrated. Recent theoretical studies in the exact diagonalization method for a finite system show that the system favors the quantum spin liquid (QSL) with an excitation gap.

Experimentally, the magnetizations for the 4/7 AFM solid ^{3}He phase adsorbed on graphite preplated by one layer of ^{4}He and bilayer of HD have been measured above 100 μK, without any clear evidence of a spin gap. Hence the ground state of the 4/7 phase is still an open question. Here the first direct demagnetization of the 2D ^{3}He down to 10 μK region is reported.

We have prepared the three different samples: (I) the paramagnetic solid ^{3}He formed on graphite as the first layer, (II) the antiferromagnetic solid ^{3}He adsorbed on one layer of ^{4}He preplated graphite, (III) the antiferromagnetic solid ^{3}He adsorbed on two layers of HD preplated graphite. They were demagnetized slowly by themselves in 17 hours from the initial condition of B_i=0.55 T and T_i=150 μK to the final field B_f= 5mT or 2.5 mT, where NMR measurements have been made to clarify their magnetization. The result from the sample (I) is essential to know the demagnetization process, because the sample temperature can be determined easily from the magnetization which obeys a Brillouin function. According to the results, the sample is rather strongly connected with the Cu nucei on the second stage and the heat bath model was proposed to explain the process. Based on it, the demagnetized temperatures of the AFM samples (II) and (III) were determined.

The magnetizations for the antiferromagnetic solid ^{3}He adsorbed on both one layer of ^{4}He and two layers of HD preplated graphite are shown in Figure 1. The data in the high temperature region are also shown there. They increase gradually down to about 10 μK. However no evidence corresponding to a spin gap was observed even for at much lower temperatures than the exchange interaction by a factor

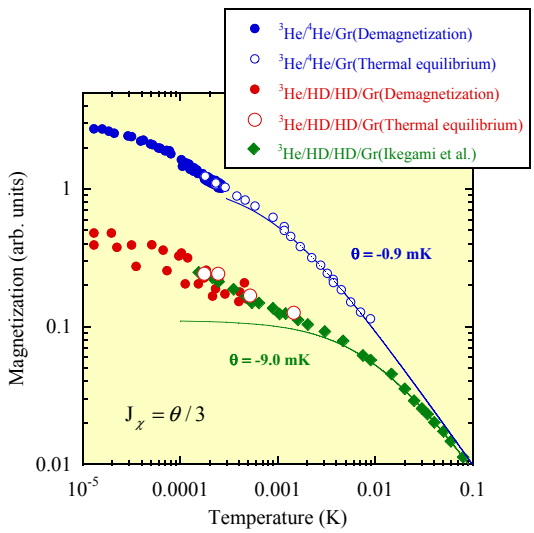

Fig.1. Temperature dependence of magnetization for 2D antiferromagnetic solid ^{3}He on mono layer of ^{4}He and bilayer of HD preplated graphite .

of almost 300, indicating a strong possibility of a quantum spin liquid ground state with zero spin gap in the 2D triangular antiferromagnetic system with the multiple spin exchange. These results are consistent with the heat capacity data observed in the second layer, but in contradiction with the theoretical prediction in the exact diagonalization for a finite size. The system size in these calculations might be too small because the higher order multiple spin exchange processes play important roles. Further theoretical calculations for a larger size of the system are eagerly desired.

Authors
Ryuichi Masutomi , Yoshitomo Karaki and Hidehiko Ishimoto

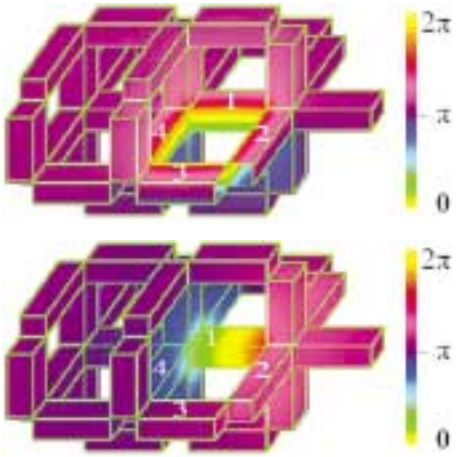

Fig. 2. η vortex ring (upper) and ξ vortex ring (lower)

Calculation of the Phase Field of a Vortex Pair on the Surface of a Multiply Connected Substrate

M. Kubota

The superfluid properties of thin ^{4}He films adsorbed on three-dimensionally (3D) connected porous media have been studied for many years. Helium films adsorbed on large-scale flat substrates are known to exhibit the classic 2D Kosterlitz-Thouless (KT) phase transition. On the other side, thin ^{4}He films adsorbed on 3D connected porous media present a number of interesting physical phenomena: dilute Bose gas behavior for low-density ^{4}He adsorbed in Vycor glass; 3D critical behavior observed for a wide range of systems; and 2D and 3D crossover behavior as a function of system structure and pore size. It is clear that one is not dealing with ideal 2D system; yet there remains the interesting question as to what extent vestigial aspects of 2D KT behavior may still be present in the superfluid behavior of the system. Although there has been a number of theoretical trials to describe this system, none of them treated the real complexity of the 3D connected system, instead they avoided this through simplifying assumptions.

We extend the work of the previous authors with a more realistic calculation of the energies for quantized vortex pairs taking into account the details of the 3D porous structure (Fig. 1). The quantum phase ϕ is calculated with regard to the position on the surface of lattice through a numerical

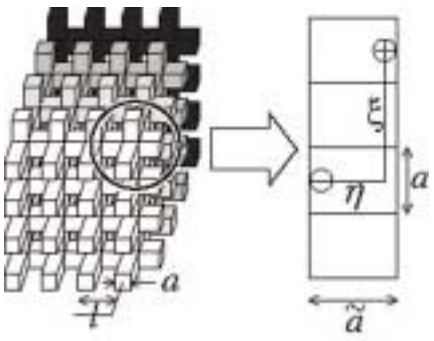

Fig. 1. The porous substrate and the development of a rod. Every rod has the same dimensions. The parameters are following: l is the lattice constant (distance between nodes), a is the thickness of a rod, $\tilde{a}=l-a$ the length of a rod, and the ξ and η are the separation around and along the rod axis, respectively. With these definitions, we define an aspect ratio $\gamma=l/a$ and the porosity $P=1-(3\gamma-2)/\gamma^3$. The open volume of the pores forms a complementary cubic structure with the same lattice parameter and the complementary aspect ratio $\gamma^*=l/\tilde{a} = \gamma/(\gamma-1)$. The entire system has a translational symmetry in each three directions.

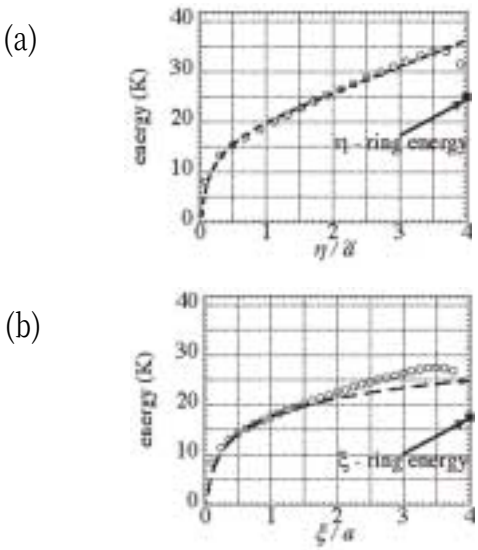

Fig. 3. The vortex pair energy functions. (a) The energy function when a vortex pair expands along the η axis. The broken line is the analytic cylinder function. (b) The energy function when a vortex pair expands along the ξ axis. The broken line is a normal KT-type logarithmic function. The squares in the panels (a) and (b) are the η and ξ ring energy, respectively (see the main text).

solution of Laplace's equation while maintaining the continuity of each rod. We place a vortex pair on a single rod and displace them. The position of a vortex "core" is defined on the smallest sites of grids by a 2π phase change. The flow field and the total energy are obtained once the phase field is calculated. Some solutions of Laplace's equation are shown on the colored graphs in Fig. 2. Flow field is defined of the special derivative of phase. There is 3D coherence of phase and the flow field is the vortex-like configuration around a pore and a rod.

We plot the energy functions with respect to the vortex configurations in Fig. 3. The vortex pair energy dependence on the displacement is similar to the classical vortex pair energy dependence in the smallest displacement. Once the vortex pair are moved further, the energy exhibits the peak. The whole process shows a thermal activation process. We calculated the porosity dependence of the energy function and concluded some calculation based on the simple mean field for excitations with a thermal activation process for a certain porosity case.

Principal Publication and Authors:
T. Obata and M. Kubota, Phys. Rev.B **66**, 140506 (2002).

Micro Pressure-Cell for Measurements of Specific Heat and Magnetization

I. Umehara, M. Hedo and Y. Uwatoko

Strongly correlated electron systems under the high pressure show a variety of physical properties. In order to understand the ground state properties of the strongly correlated electron systems under high pressures, many different piston cylinder type high pressure cells have been designed. (See for example Ref. [1]) We have developed a micro pressure-cell for the measurements of specific heat and magnetization, which can be used in the commercial SQUID magnetometer. Here we report about the design of our micro pressure cell.

Figure 1 shows the schematic drawing of the micro cell. The cylinder and upper and lower nuts of the micro pressure cell are constructed from hardened CuBe alloy (C1720B-H). The dimensions of the cylinder are 8.8, 2.7 and 21 mm for the outer diameter, inner diameter and length, respectively. ZrO_2 was used for the piston and piston backups. The high-pressure sample space was sealed by Teflon cell technique with Cu seal rings. The mixture of Fluorinert FC70:FC77 =1:1 was used as the pressure transmitting media. Total weight of this cell is about 9 g. To the best of our knowledge, our cell is one of the smallest among this type. Using some attachments as drawn in the figure, it can be used for the specific heat and magnetization measurements. The magnetization studies were performed with commercial SQUID magnetometer and the specific heat measurements were carried out using the conventional adiabatic method. In preparation for the specific heat measurements, we have measured the heat capacity of the micro pressure-cell with the mixture of Fluorinert under several pressures. We have also measured the magnetization of our cell as functions of temperatures and magnetic fields.

As an example, we show in Fig. 2 the specific heat (top) and the magnetization (bottom) as a function of temperature below 9 K for the single crystalline CeAg under various pressures, 0, 0.30, 0.83, and 1.37 GPa. In this experiment, the weight of the sample is 80 mg, which is less than 1 % of the weight of the pressure cell. However, the heat capacity of the sample at around 8 K is about 20 % of the total heat capacity. For the magnetization measurements, a magnetic field of 100 Oe was applied along the ⟨100⟩ direction in a Cubic notation at room temperature. The Curie temperature T_C increases with pressure below around 0.6 GPa and then decreases with increasing pressure up to 1.37 GPa. The T_C values determined from the specific heat and the magnetization measurements are in excellent agreement with each other and with previous resistivity measurements [3,4]. We have succeeded in applying pressures up to 2 GPa (low temperature value) in other experiments with our cell. Detailed analysis of our measurements for the specific heat and the magnetization in CeAg will appear elsewhere.

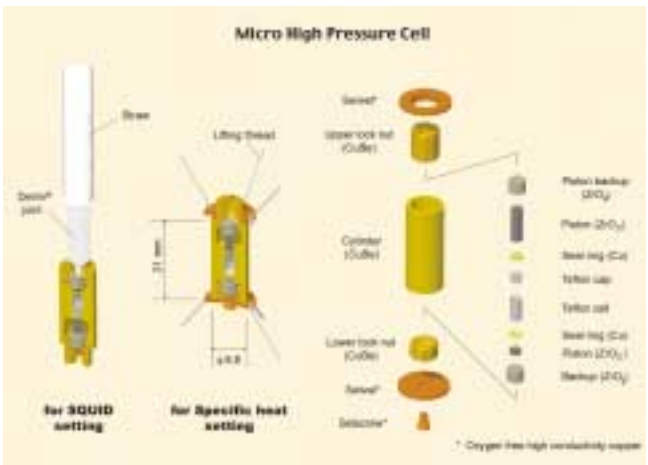

Fig. 1. Schematic drawing of micro pressure cell.

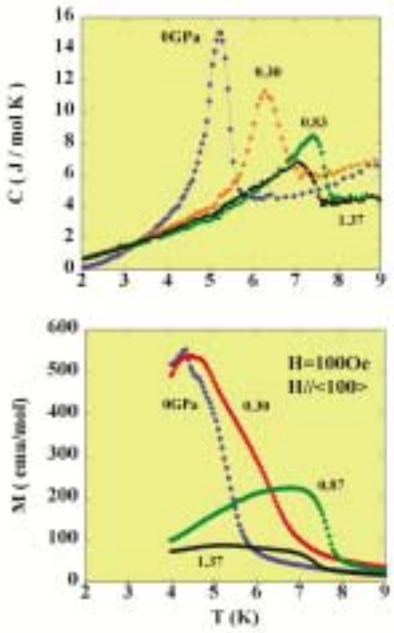

Fig. 2. The specific heat and magnetization for CeAg as a function of temperature at various pressures.

References

[1] Y. Uwatoko *et al*., Rev. High Pressure Sci. Technol.**7**, 1508 (1998).
[2] P. Morin, J. Magn. Magn. Mater. **71**, 151 (1988).
[3] M. Kurisu, J. Phys. Soc. Jpn. **56**, 4064 (1987).
[4] A. Elling and J.S. Scilling, Phy. Rev. Lett. **46**, 364 (1981).

Authors
Izuru Umehara[a], Masato Hedo, Yoshiya Uwatoko
[a]Division of Physics, Faculty of Engineering, Yokohama National University.

World Record Fast Rotating ULT Cryostats

T. Mizusaki and M. Kubota

Superfluidity is a macroscopic quantum phenomena where the phase of the condensate or bulk superfluid is a macroscopic physical quantity and can be controlled by external flow or rotational motion of the vessel. Since the first observation of the meniscus of the rotating superfluid ^{4}He by Osborn, experiments under rotation brought us continued surprises [1]. This first observation led to the idea of Onsager-Feynmann vortex lines. Henry Hall was the first to observe persistent superflow after rotation, and W.F. Vinen found that the flow around a wire is quantized with a circulation given by h/m, where h is Plank's constant and m is the ^{4}He atom mass. Since then, there have been a number of experiments performed under rotation for ^{4}He. Superfluid made of Fermi particle, ^{3}He has been studied under rotation since 80's [2]. Kubota and his group have been studying till present time a new class of 3D superfluid; submonolayer

Fig. 1. ISSP ULT Rotation Cryostat with rotating scheme Tok-01. Two high precision air bearing units are located at the ends of the shaft. Electronics are located on a table above and driven by precision motor through timing belt. The connection between this table and the shaft which connects rigidly the cryostat is made by a soft torsion rod, which functions also as a rotational vibration isolator. Earth field cancellation coils are seen on a thick paper cylinder around the Dewar.

^{4}He film systems condensed on 3D connected surface of porous substrates. And some experiments have been performed under rotation [3]. Now we are adding ourselves to the groups of ^{3}He study under rotation, as well, after ones at Cornell, Helsinki, Berkeley, and Manchester: Ishiguro *et al.* have reported vortex nucleation and textures in small cylinders [4], which indicates an interesting features of this anisotropic superfluid made of Cooper pairs with large internal freedom.

Rotation for the study of superfluids is compared sometimes with magnetic field for the study of superconductors. Rotational speed, for example, to destroy superfluidity can be compared with critical magnetic field H_{c2}, but as to rotation, it has been far beyond reach of the present known technology to overcome H_{c2} correspondance for T=0 K for bulk superfluids. We are, however, making some progress and under some conditions of combination of the new high speed rotating cryostat (Fig.2) and the artificial 3D superfluid consisting of thin He film and porous media we may come close to cover interesting phase fields of a superfluid.

References

[1] see for example, E.L. Andronikashvili and Yu.G. Mamaladzs, Rev. Mod. Phys. **39**, 567 (1966).
[2] O. Lounasmaa and E. Thuneberg, Proc. Nat. Acad. Sci. USA, 96 (1999).

Fig. 2. ISSP High Speed Rotating Cryostat. Experiments under up to 6 rotation/sec are tested at dilution refrigerator temperatures.

[3] M.K. Zalalutdinov *et al.*, Czechoslovak J. Phys. **46**, S1-39 (1996); M. Fukuda *et al.*, J. Low Temp. Phys. **113**, 417 (1998); M. Fukuda *et al.*, Physica B **250-252**, 117 (2000).
[4] R. Ishiguro *et al.*, Physica B **329-333**, 66 (2003).

Principal Publication and Authors

Minoru Kubota, Toshiaki Obata, Ryousuke Ishiguro, Minoru Yamashita,Takeshi Igarashi, Emi Hayat, Osamu Ishikawa, Yutaka Sasaki, Nikolay Mikhin; Muneyuki Fukuda, Vladimir Kovacik , Takao Mizusaki, Physica B **329-333**, Part 1, 577 (2003).

Trajectory of the Wave Packets Oscillating on an Adiabatic Potential Surface

T. Suemoto

Real time tracking of the movement of atoms is a fundamental desire in investigating the ultrafast lattice rearrangement phenomena in solids. In this study, we have shown that the real time tracking of precise spatial positions of atoms is possible by using a luminescence method.

The self-trapped excitons (STE) are generated by 20 fs light pulses at 1.6 eV in quasi-one-dimensional halogen-bridged platinum complex $[Pt(en)_2]$ $[Pt(en)_2Br_2](ClO_4)_2$ (en=ethylendiamine). Previously, we observed intensity modulation of the luminescence with a period of about 290 fs [1], corresponding to the oscillations of the wave-packets on the adiabatic potential curve of the lowest STE state (see the black dots in Fig. 1).

We have greatly improved the experimental setup for the up-conversion spectroscopy and performed a measurement with a time resolution of about 40 fs, which we believe is the best value ever achieved. At a photon energy of 0.8 eV, which corresponds to the luminescence from the bottom of the adiabatic potential curve, we observed the overtone modulation with a period of about 145 fs as shown in Fig. 1 by green arrows. This has not been seen in the measurement with 90 fs time resolution, while it was theoretically expected to be observed if the time resolution is improved [1]. Modulation frequency was doubled, because the wave-packet passes thorough the bottom of the adibatic potential curve

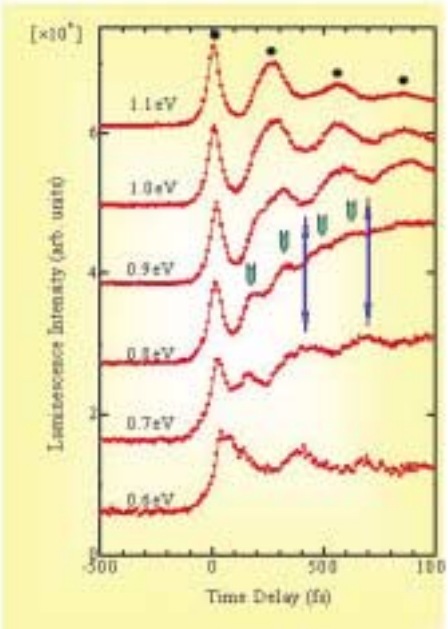

Fig. 1. Time evolution of the luminescence intensity at various photon energies. At 1.1 eV, the oscillation period corresponds to that of the wave packet motion. At 0.8 eV overtone oscillation is observed.

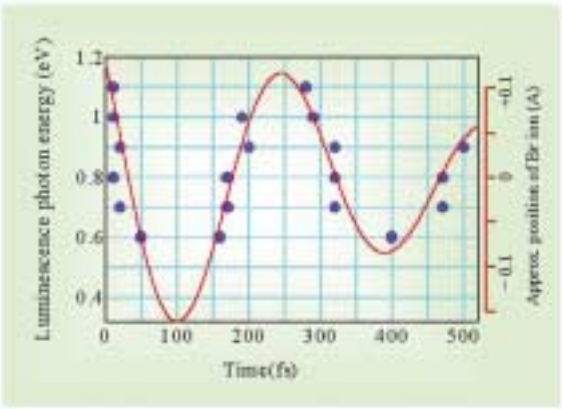

Fig. 2. The positions of the peaks and shoulders in the time evolution curves in Fig. 1 are shown by blue circles on the coordinates of time and photon energy. The scale on the right side shows the approximate displacement of the Br from the equilibrium position. The red curve shows the motion of the peak of the wave packet assuming a damped harmonic oscillator.

twice within one period in alternative directions. We can see also the anti-phasing behavior between the oscillations of luminescence at the photon energies of 0.7 eV and 0.9 eV (shown by blue arrows). The luminescence at these two energies probes the wave-packet at the points on the opposite sides of the potential minimum. This clearly shows that the wave-packet is moving back and forth around the potential minimum. The peaks or the shoulders in each curve corresponds to the moment when the peak of the wave packet passes on the point corresponding to the observed photon energy. Thus we can make a trajectory of the wave packet moving in the adiabatic potential curve by plotting the peak points as shown in Fig. 2. If we assume the same curvature for the ground state and the excited state, the luminescence energy can be directly translated into the position of the oscillating ion (Br in this case). Thus we succeeded in tracking the spatial positions of atoms [2].

References
[1] S. Tomimoto et. al., Phys. Rev. B **60**, 7961 (1999).
[2] T. Matsuoka, S. Saito, J. Takeda, S. Kurita, and T. Suemoto, Nonlinear Optics **29** (10-12), 587-593 (2002).

Authors
Taira Matsuoka, Tohru Suemoto, Jun Takeda[a] and Susumu Kurita[a]
[a] Yokohama National University

Three-Dimensional Imaging of Ge Atoms on Si(001) by Using a Holographic Method in X-ray Diffraction

T. Takahashi

In X-ray diffraction what we can observe is X-ray intensities, and thus the phase of X-ray waves is lost in measurements. If, however, we can get the information of phases of diffracted X-rays, the atomic structure of materials is reconstructed from intensity data through Fourier transform.

In the present work, we show a holographic method to reconstruct images of surface and interface atoms with an atomic resolution. Here we treat two-dimensionally ordered atoms on a substrate crystal. Hitherto similar attempts have been made as to two-dimensional structures projected on the surface. In this work, in contrast, we show the first experimental result of three-dimensional reconstructed images of

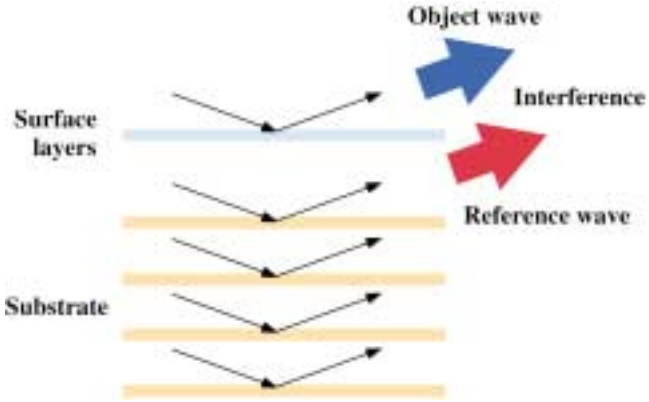

Fig. 1. Principle of the present method to reconstruct images of surface atoms using an interference effect.

surface atoms.

Figure 1 illustrates the principle of the present method. In this case the diffraction amplitude from a sample is divided in two; one is a contribution from a surface layer to be determined, and the other is a contribution from a substrate crystal given by the sum of amplitudes from a semi-infinite layers. In most cases we know the structure of the substrate crystal, and can calculate the phase and modulus of the amplitude based on the X-ray diffraction theory. Thus we can regard the wave scattered from the substrate crystal as a reference wave. In this situation, we can reconstruct unknown surface atoms by a Fourier transform after a proper normalization of the experimental data, instead of illuminating a reference wave as in optical holography.

Figure 2 shows images of Ge atoms on Si(001) substrate crystal reconstructed from observed intensities. Here we used a sample in which a monolayer of Ge atoms are epitaxially grown on a clean Si(001) surface at 775 K. A few nanometers of an amorphous Si layer was further deposited on the sample at 295 K to treat in the atmosphere. To reconstruct the images, we have obtained intensities about at 250 points, most of which are measured at points on the crystal-truncation rod close to Bragg points. The result clearly shows that Ge atoms locate positions that Si atoms would otherwise occupy. The position of Ge atoms is slightly relaxed toward the surface, reflecting the difference in bond lengths between Ge and Si in crystals.

In the structure analysis of surfaces and interfaces, constructing an initial model is a most elaborating task. Thus

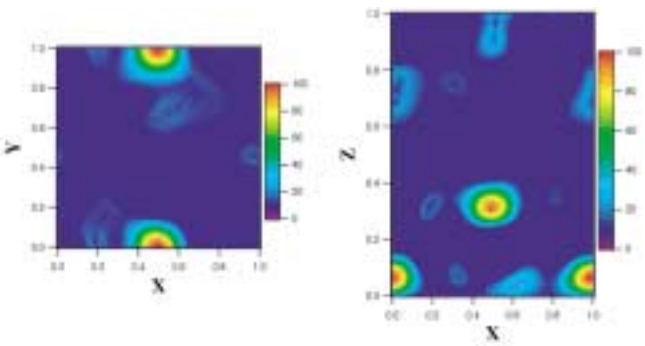

Fig. 2. Contour maps of Ge atoms on Si(001) substrate crystal at planes parallel (left) and perpendicular (right) to the surface. Rectangular regions indicate the unit cell defined so that only a single atom is included in a plane parallel to the surface.

once the initial structure is directly obtained from experimental data, one could easily refine the structure, with for instance, the use of conventional fitting procedures. Combination of the present method with direct methods will be more promising.

Principal Publication and Authors
K. Sumitani, T. Takahashi, S. Nakatani, A. Nojima, O. Sakata, Y. Yoda, S. Koh, T. Irisawa, and Y. Shiraki; Jpn. J. Appl. Phys. **42**, L189-L191 (2003).

Discovery of Missing Link: III. The *A*-site Ordered Manganese Perovskite $RBaMn_2O_6$

Y. Ueda

The manganese perovskite $R^{3+}_{1-x}A^{2+}_xMnO_3$ has drawn much attention in its rich physical properties such as ferromagnetic metal (FM) generated by the double-exchange interaction, charge/orbital order (CO), colossal mangetoresistence and electronic phase segregation. It is now widely accepted that these interesting phenomena are caused by the strong correlation/competition of multi degrees of freedom, that is, spin, charge, orbital and lattice, and could be significantly influenced by the *A*-site randomness. Although the search for the compound without the *A*-site randomness has been motivated by its intriguing properties, it has been missing in manganese perovskites.

Recently, the *A*-site ordered manganese perovskite $RBaMn_2O_6$ (*R* = Y and rare earth elements) has successfully synthesized and investigated in the structure and electromagnetic properties. The most significant structural feature of $RBaMn_2O_6$ is that the MnO_2 square sublattice is sandwiched by two types of rock-salt layers, *R*O and BaO, with much different sizes and consequently the MnO_6 octahedron itself is heavily distorted. The electromagnetic properties are summarized in Fig. 1 as an electronic phase diagram. Compared with the *A*-site disordered $R_{0.5}A_{0.5}MnO_3$ (*A* = Sr, Ca), $RBaMn_2O_6$ displays remarkable features: (1) the CO transition at T_{CO} far above 300 K, (2) a new stacking variation of the CE-type CO with a 4-fold periodicity along the *c*-axis (4CE-CO), (3) the presence of structural transition possibly accompanied by $d_{x^2-y^2}$ orbital order at T_t above T_{CO}, and (4) the electronic phase segregation. The relatively high T_{CO} and the absence of critical region can be understood as the effect of the absence of *A*-site randomness. The 4CE-CO could originate from the layer-type order of *A*-site cations. The structural transition at T_t is the most remarkable feature in $RBaMn_2O_6$. The large mismatch between *R*O and BaO lattices introduces a strong frustration to the MnO_2 sheet and must give a new perturbation to the competition of multi-degrees of freedom among charge, orbital, spin and lattice. The last feature, that is, the coexistence of FM and CO phases as the ground state in $LaBaMn_2O_6$ far from CO state, might be explained as the effect of the elongation of Mn-O-Mn distance (reduction of bandwidth). Such effect has never been seen in ordinary $R^{3+}_{1-x}A^{2+}_xMnO_3$.

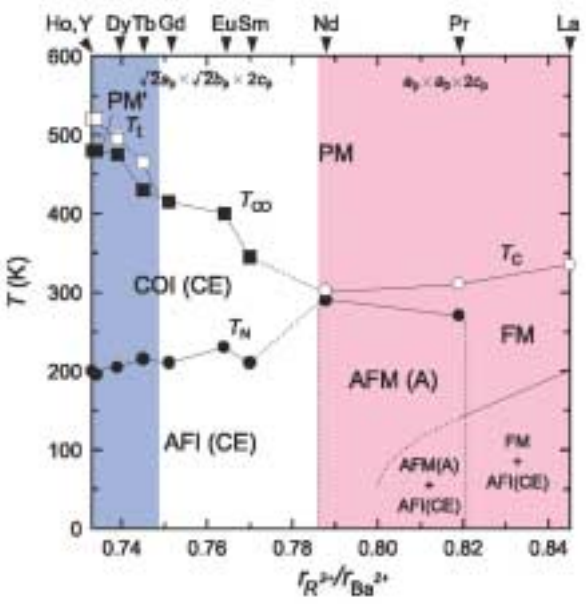

Fig. 1. Phase diagram for $RBaMn_2O_6$ expressed as a function of the ratio of ionic radius, $r_{R^{3+}}/r_{Ba^{2+}}$. The *A*-site ordered manganites $RBaMn_2O_6$ can be classified into three groups from the structural and electromagnetic properties. The first group (*R* = Y, Tb, Dy and Ho) shows successive three phase transitions, structural transition, charge/orbital order (COI) and antiferromagnetic order (AFI), on cooling. The second group (*R* = Sm, Eu and Gd) exhibits a COI transition, followed by an AFI. The third group (*R* = La, Pr and Nd) has a ferromagnetic metal (FM) transition, followed by an *A*-type AF (AFM) in $PrBaMn_2O_6$ and $NdBaMn_2O_6$. The electronic phase segregation is observed in $LaBaMn_2O_6$.

Principal Publication and Authors
T. Nakajima, H. Kageyama, H. Yoshizawa and Y. Ueda, J. Phys. Soc. Jpn. **71**, 2843 (2002).

Photocarrier Injection to a Transition Metal Oxide

Z. Hiroi

An efficient method to dope a transition metal oxide (TMO) with hole carriers is presented, which is photocarrier injection (PCI) in an oxide heterostructure. It is shown that an insulating vanadium dioxide (VO_2) film is rendered metallic under light irradiation by PCI from an *n*-type titanium dioxide (TiO_2) substrate doped with Nb. Consequently, large photoconductivity, which is exceptional for TMOs, is found in the VO_2/TiO_2:Nb heterostructure. We propose an electronic band structure where photo-induced holes created in TiO_2:Nb can be transferred into the filled V 3*d* band via the low-lying O 2*p* band of VO_2.

We have fabricated a 10-nm-thick VO_2 film epitaxially grown on the (001) surface of a Nb-doped TiO_2 single crystal substrate with nominal Nb concentration of 0.05 wt%. The deposition was carried out in a vacuum chamber using a pulsed laser deposition technique with a KrF excimer laser (λ=248 nm) and a V_2O_3 pellet as a target.

Figure 1 shows the temperature dependence of in-plane resistance measured in the dark and under light irradiation. In the dark, a large jump in resistance is observed at *T* = 297 K on heating and *T* = 287 K on cooling due to the MI transition: The T_{MI} is lower by 40 K than that of a single crystal. The thermal hysteresis is due to the first-order nature of the phase transition. When the sample is irradiated by an UV light (λ=300~400 nm), the resistance shows a small jump at almost the same T_{MI} as in the dark. Surprisingly observed below T_{MI} is a dramatic reduction in resistance by more than two orders of magnitude. In addition, the resistance decreases gradually with decreasing temperature, indicating a metallic behavior, in contrast to an

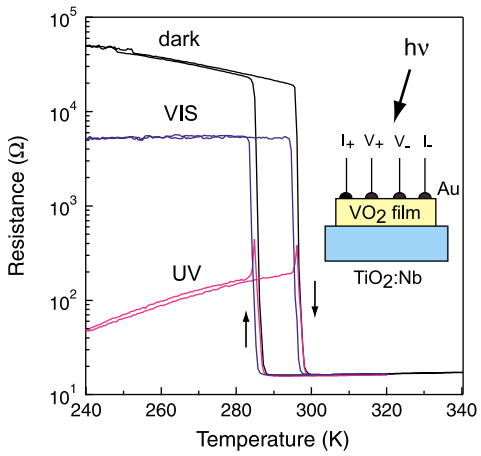

Fig. 1. Temperature dependence of in-plane resistance measured on cooling and heating. The sample is a 10-nm-thick VO_2 film grown on an *n*-type TiO_2:Nb (nominally 0.05 wt%) substrate with 0.5 mm thickness. An ultraviolet (UV) light (wavelength: 300-400 nm; irradiance: 140 mWcm^{-2}) or a visible (VIS) light (wavelength: 400-700 nm; irradiance: 350 mWcm^{-2}) from a xenon lamp was guided via an optical fiber to irradiate the sample during the measurements.

insulating temperature dependence seen in the dark. We also detected a small reduction of about 4 % in resistance above T_{MI}. On the other hand, a similar but smaller reduction is observed for visible-light irradiation. These photoconductivity occurs quite reversible upon light switching.

We propose a simple picture for the electronic structure of the VO_2/TiO_2:Nb system to explain the experimental facts qualitatively (Fig. 2). It is well established that TiO_2 possesses a valence band of nearly O 2*p* orbital character and a conduction band of Ti 3*d* character. Nb^{5+} donor levels exist just below the conduction band. On the other hand, VO_2 has a nearly half-filled $d_{//}$ band in the metallic phase which splits into two, $d_{//}$ and $d_{//}^*$ bands, in the insulating phase. To combine the two materials into a junction, assuming Fermi level matching, results in almost uniquely the energy diagrams shown in Fig. 2 for two situations; one at high temperature above T_{MI} in the dark and the other at low temperature below T_{MI} under UV light irradiation. It is to be noted that the band structure of the junction would be completely different without donors in TiO_2, because the Fermi

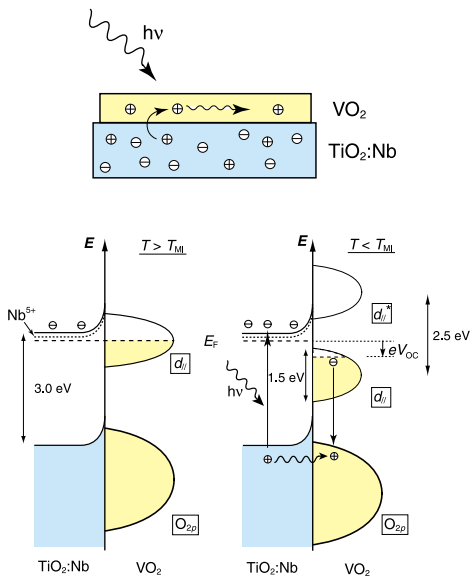

Fig. 2. Schematic drawings of photocarrier injection (PCI) from a TiO_2:Nb substrate to a VO_2 film under light irradiation and of the electronic structure for the VO_2/TiO_2:Nb heterostructure.

level would lie in the middle of the gap of TiO_2 in that case.

Light absorption should occur mostly in the thick (0.5 mm) TiO_2:Nb crystal, creating holes and electrons in the valence and conduction bands, respectively. Then, it is naturally expected from the energy diagram for the low-temperature case that only the holes can migrate into the O 2*p* band of VO_2, because the top of the O 2_p band of VO_2 is located slightly above that of the valence band of TiO_2:Nb, while the bottom of the empty $d_{//}^*$ band of VO_2 is much above that of the conduction band of TiO_2:Nb. A possible upward bending of the TiO_2 bands near the interface may help this electron-hole separation. With increasing hole density in VO_2, the VO_2 bands should shift downward by an induced open-circuit voltage V_{OC} which was in fact detected in our transverse voltage measurement across the interface. The transferred holes in the O 2*p* band of VO_2 must find their counter electrons located near the Fermi level to be combined, resulting in conducting hole carriers in the $d_{//}$ band at low temperature below T_{MI}. As a result, the VO_2 film becomes a metal, exhibiting a large photoconductivity or an insulator-to-metal transition under light irradiation.

The present PCI method would provide us with an efficient and convenient way for tunable hole doping in many TMOs. From the physical point of view, PCI would be very interesting to test the effect of 'clean' hole doping. On the other hand, from the application point of view, the present heterostructure could be used as a new type of optoelectronics device using an UV light.

Principal Publication and Authors

Y. Muraoka, T. Yamauchi, Y. Ueda and Z. Hiroi; J. Phys.: Condens. Matter **14**, L757 (2002).

Novel In-gap State in Zn-doped $La_{1.85}Sr_{0.15}CuO_4$

K. Hirota

It is a received wisdom that the antiferromagnetism (AF) on a hole-doped CuO_2 plane in a lamellar copper oxide is relevant to the high T_c superconductivity. Our aim is to understand the spin state of doped CuO_2 plane, particularly in the superconducting state. However, there exists no AF long-range order (LRO), and the low-energy spin excitations, which might play an important role in the high T_c superconductivity, disappear due to a so-called *spin gap* at low temperatures. The best way to observe the low-energy spin response is to suppress the superconductivity by giving some perturbations to the spin system without changing the other properties. Zn doping is extremely suitable for the purpose: A small amount of Zn^{2+} ions substituting for Cu^{2+} ions strongly suppress the superconductivity without doping holes nor giving much structural disturbance. NMR and neutron studies have revealed that doped Zn impurities induce staggered magnetic moments on the surrounding Cu sites, indicating that Zn-doping enhances AF correlations on a CuO_2 plane [1,2]. If we can tune T_c by precisely controlling the Zn concentration in single crystals large enough for inelastic neutron scattering, it would provide a chance to study in detail the microscopic nature of spin correlations and their contribution to the high T_c paring mechanism.

We have carried out a comprehensive neutron scattering study of the AF spin correlations in Zn-doped $La_{1.85}Sr_{0.15}CuO_4$ single crystals to elucidate how the spin-

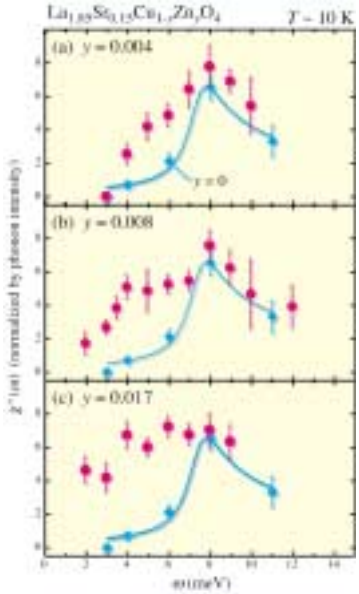

Fig. 1. Energy dependence of the q-integrated $\chi''(\omega)$ for (a) y=0.004, (b) y=0.008 and (c) y=0.017 at 10 K. Open diamonds denote the data for y=0.0. Solid lines are fits with a phenomelogical dynamical spin susceptibility.

gap state is broken and how the static AF correlations are induced by Zn-doping. To obtain quantitative information about the Zn-doping dependence of spin excitation spectra, it is essential to control the Zn-doping rate accurately. Furthermore, large and spatially homogeneous crystals are required. We have overcome such difficulties by combining the traveling-solvent-floating-zone (TSFZ) method and a quantitative analysis of elements using the inductively-coupled plasma method. Our systematic studies with changing the Zn-doping rate under *unified* experimental conditions revealed a novel low-energy spin excitation which is induced within the spin gap state by doped Zn impurities.

Figure 1 shows the energy spectra of the dynamical spin susceptibility $\chi''(\omega)$ around 10 K. All the data are corrected so as to be directly compared. It is remarkable that $\chi''(\omega)$ for all the samples have a maximum and almost identical intensity around ω = 8 meV, while $\chi''(\omega)$ below 8 meV develops with increasing doped Zn. These systematic changes cannot be explained by either the broadening of the gap structure or the reduction of the gap-energy because both the cases should be associated with the variation of $\chi''(\omega)$ near the gap energy. Therefore, these energy spectra indicate that Zn-doping induces an *additional* spin excitation in the spin gap below ω~8 meV and that, with further doping, the novel spin excitation is enhanced and shifts to lower energies, i.e., becomes more static. Indeed, the elastic magnetic signals were observed for y=0.017 below ~20 K at the same incommensurate positions as that of the inelastic scattering, while no signal was detected in y=0.008 down to 1.5 K. The in-plane spin correlation length for y=0.017 is estimated at ~80 Å.

A mean distance between Zn ions ($R_{Zn\text{-}Zn}$) shortens from ~60 Å in y=0.004 to ~42 Å in y=0.008. We thus speculate that the induced local magnetic moments around a doped Zn ion start correlating with those around other Zn ions for y=0.008, and that the correlations among the moments around different Zn ions become coherent, which gives rise to the novel in-gap spin state at particular q positions. The in-plane *static* spin correlation lengths for y=0.014 and 0.017 exceed 80 Å, which is much longer than their $R_{Zn\text{-}Zn}$ values, 32 and 29 Å. This fact indicates that the static spin correlations originate not from the independent local magnetisms around Zn impurities *but* from the long-range AF coherence among the induced moments around different Zn ions. Thus we conclude that the in-gap state continuously connects with an AF ground state with increasing Zn, i.e., decreasing $R_{Zn\text{-}Zn}$, indicating the importance of underlying AF ground state which is locally substituted for the superconducting state with help of small perturbations.

References
[1] M.-H. Julien *et al*., Phys. Rev. Lett. **84**, 3422 (2000).
[2] K. Hirota, Physica C **357-360**, 82 (2001).

Authors
H. Kimura[a], M. Kofu and K. Hirota
[a]IMRAM, Tohoku University

Measurement of an Electron Beam Size with a Beam Profile Monitor Using Fresnel Zone Plates

N. Nakamura

In low-emittance accelerators such as third-generation synchrotron light sources and linear-collider damping rings, the beam size reaches less than ten micrometers. A beam profile monitor with an x-ray imaging optics for synchrotron radiation (SR) is expected to measure such a small electron-beam size with a high spatial resolution in a non-destructive manner. A Fresnel zone plate (FZP) begins to be used as an x-ray imaging lens and its spatial resolution, which depends on the outermost-zone width of the FZP, is capable of being less than 100 nm. A real-time beam profile monitor based on FZPs was already proposed and designed for the Super-SOR light source [1]. We have recently constructed the same type of beam profile monitor in the KEK-ATF damping ring with an emittance of about 1 nm to study the feasibility of the monitor.

Figure 1 shows the layout of the beam profile monitor system constructed in the KEK-ATF damping ring. The monitor system has a structure of a long-distance x-ray microscope, where two FZPs (CZP: Condenser Zone Plate and MZP: Micro Zone Plate) constitute an x-ray imaging optics. The synchrotron radiation from the electron beam at the bending magnet is monochromatized by a Si(220) crystal monochromator and the electron beam profile is twenty-times magnified by two FZPs and detected on an x-ray CCD camera. The spatial resolution is about 1.7 μm for the selected photon energy of 3.235 keV. The x-ray CCD camera is a direct incident type with a back-thinned illuminated CCD, which offers high quantum efficiency, more than 90 % for the selected x-ray energy.

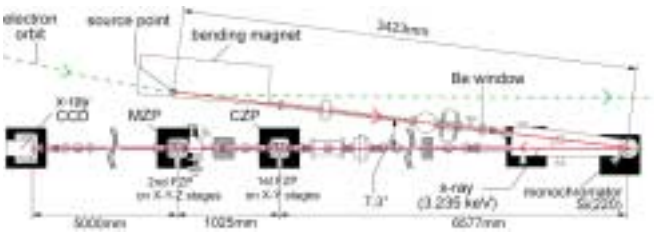

Fig. 1. Layout of the beam profile monitor system.

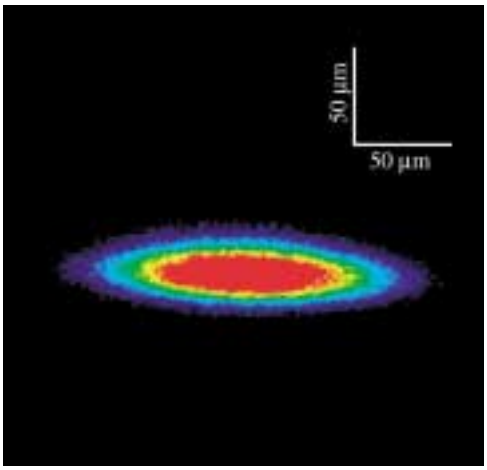

Fig. 2. Electron beam image obtained by the beam profile monitor. The horizontal and vertical bars of 50 µm reflect the dimension at the SR source point.

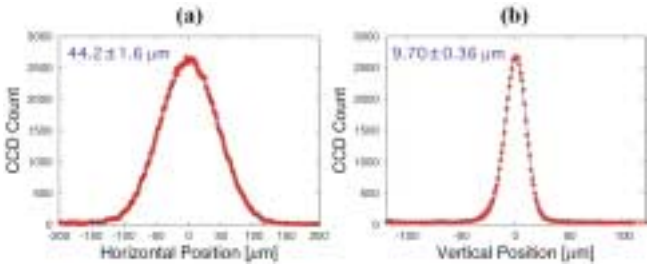

Fig. 3. (a) horizontal and (b) vertical beam profiles with their fitted gaussian curves. The axes of abscissa use the dimension at the SR source point.

Figure 2 shows a typical electron-beam image measured by the beam profile monitor. The horizontal and vertical sizes were obtained by fitting the horizontal and vertical profiles of the beam image to gaussian curves. Figure 3 shows the horizontal and vertical beam profiles and their fitted gaussian curves. The beam sizes were measured on five different days with different beam currents and tuning conditions of the ring. The obtained horizontal beam sizes were about 40 mm and the vertical beam sizes 7 - 10 µm. With this monitor, we have succeeded in obtaining a clear electron-beam image and measuring the electron-beam size less than 10 µm. The good performance and prospects of the monitor were confirmed in the experiments.

Reference

[1] N. Nakamura et al., Proc. of the 2001 Particle Accelerator Conference, Chicago, 2001, p. 1628-1630.

Authors

N. Nakamura, K. Iida, H. Sakai, K. Shinoe, H. Takaki, M. Fujisawa, H. Hayano[a], M. Nomura[a], Y. Kamiya[a], T. Koseki[b], Y. Amemiya[c], N. Aoki[d], K. Nakayama[d]

[a]High Energy Accelerator Research Organization(KEK)
[b]Institute of Physical and Chemical Research(RIKEN)
[c]Graduate School of Frontier Sciences, University of Tokyo
[d]Toshiba Corporation